Search for the Higgs boson in $H \to WW$ decays in vector boson fusion with ATLAS at the LHC

Suche nach dem Higgs boson in $H \to WW$ Zerfällen in Vektor-Boson-Fusion mit ATLAS am LHC

Masterarbeit an der Fakultät für Physik
der
Ludwig-Maximilians-Universität München

vorgelegt von
Nikolai Hartmann
geboren in Starnberg

München, den 6.10.2014

Gutachter: PD Dr. Johannes Elmsheuser

Abstract

This thesis describes the search for a standard model Higgs boson at a mass of 125 GeV in $H \to WW$ decays in vector boson fusion production using ATLAS $\sqrt{s}$ =7 TeV data. The signal region is defined with a cut based approach. The goal is a combination with a similar analysis of $\sqrt{s}$ =8 TeV data from which the present analysis is derived. Modifications have been made to account for the lower statistics in the $\sqrt{s}$ =7 TeV dataset. The expected significance for the $\sqrt{s}$ =7 TeV analysis alone is 0.82σ. The observed significance is 0.08σ at a signal strength of $0.16^{+1.8}_{-1.2}$. The combination with the $\sqrt{s}$ =7 TeV analysis increases the expected sensitivity of the $\sqrt{s}$ =8 TeV analysis by 6%. The combined expected significance is 2.1σ. The observed significance is 3.0σ with a signal strength of $1.5^{+0.8}_{-0.6}$.

Zusammenfassung

Diese Arbeit beschreibt die Suche nach einem Standard Modell Higgs-Boson mit einer Masse von 125 GeV in $H \to WW$ Zerfällen in Vektor-Boson-Fusion mit ATLAS $\sqrt{s}$ =7 TeV Daten. Die Signalregion wird über einen schnittbasierten Ansatz definiert. Das Ziel ist eine Kombination mit einer vergleichbaren Analyse von $\sqrt{s}$ =8 TeV Daten von der die vorliegende Analyse abgeleitet ist. Es wurden Änderungen vorgenommen um der niedrigeren Statistik des $\sqrt{s}$ =7 TeV Datensatzes gerecht zu werden. Die erwartete Signifikanz für die $\sqrt{s}$ =7 TeV Analyse separat beträgt 0.82σ, die beobachtete beträgt 0.08σ bei einer Signalstärke von $0.16^{+1.8}_{-1.2}$. Die Kombination mit der $\sqrt{s}$ =7 TeV Analyse erhöht die erwartete Signifikanz der $\sqrt{s}$ =8 TeV Analyse um 6% . Die kombinierte erwartete Signifikanz beträgt 2.1σ. Die beobachtete Signifikanz beträgt 3.0σ bei einer Signalstärke von $1.5^{+0.8}_{-0.6}$.

"Hofstadter's Law: It always takes longer than you expect, even when you take into account Hofstadter's Law."

Gödel, Escher, Bach
Douglas Hofstadter

Contents

Chapter 1

Introduction

Physics can be seen as a science that gives a fundamental description of the world. The search for this description revealed more and more fascinating properties throughout the history of research. Two of the undoubtedly most fascinating features discovered in the last century are relativity and quantum mechanics. The idea of a theory of all matter and its interactions in a relativistic quantum mechanical description lead in an iterative interplay between theory and experimental observations to the standard model of particle physics. This model is despite its limitations at the present moment the best experimentally verified fundamental theory of our world.
Until 2012 one observable component of the standard model of particle physics - the Higgs boson - was a missing piece. It is a prediction of the mechanism that gives mass to elementary particles. On 4 July 2012 the two multi purpose detectors ATLAS and CMS at the Large Hadron Collider published their search results that correspond to an observation of a signal that is consistent with the expectations for the standard model Higgs boson. The next step of establishing the signal or finding deviations from the standard model expectations is the measurement of the properties of the new particle. One of the standard model predictions are the couplings to other particles, resulting in different branching ratios (decay probabilities). The decay $H \rightarrow WW$ is one of these decay modes. By combining this with the vector boson fusion (VBF) production mode a characteristic signal is expected. In addition, the VBF $H \rightarrow WW$ process involves only couplings of the Higgs boson to the electroweak W and Z bosons which gives direct access to these couplings.
This thesis describes an analysis of proton-proton collision ATLAS data from 2011 with a centre of mass energy of 7 TeV for the VBF $H \rightarrow WW$ process. A search region enhanced in the signal is defined using a cut based approach.

Chapter 2

Theory

This chapter gives a brief introduction to the theoretical concepts of the experimental analysis in this thesis.

2.1 The Standard Model

The Standard Model (SM) of particle physics is up to now the most fundamental description of all matter in the universe which has been experimentally verified in a wide range of observations."Matter" is described to consist of fermions called leptons and quarks. "Forces" are described by the exchange of bosons.
Matter is classified in 3 generations. The particle masses increase from generation to generation (see tables 2.1, 2.2). For each particle there exists an antiparticle with opposite/negative charge like quantum numbers. This is a direct consequence of the SM being a relativistic quantum field theory.
Each generation contains an electrically charged lepton (electron, myon, tauon) with charge $+1e$ and an associated uncharged neutrino. While the charged leptons carry a mass, the neutrinos are described as massless particles in the SM (as described here). Observations of neutrino oscillations indicate that neutrinos have a non-vanishing mass. Electron neutrino masses are expected to be smaller than 2.3 eV (95% CL) from "direct" measurements using tritium β decay [1] and $\sum m_\nu < 0.23$ eV from cosmological constraints [2].
Quarks have a colour charge (called red, green, blue) which is the charge associated to the strong interaction. There exist bound states of three quarks called baryons and of a quark and an antiquark called mesons. For example protons and neutrons are baryons, pions and kaons are mesons. Each generation of matter contains one "up-type" quark and one "down-type" quark. Up-type quarks carry an electric charge of $+\frac{2}{3}e$, down-type quarks $-\frac{1}{3}e$. The quarks are named up- and down-, charm- and strange-, top- and bottom quarks

for the first, second and third generation.
The SM describes three Forces - the strong interaction, the electromagnetic interaction and the weak interaction. The strong interaction is mediated by gluons carrying a colour charge which consists of a colour and an anticolour. Gluons are massless vector (spin-1) bosons. The electromagnetic interaction is mediated by photons which are neutral massless vector bosons that couple to the electric charge. The weak interaction is mediated by the massive W (electrically charged) and Z (neutral) vector bosons. The observed masses are:

$$m_W = 80.385 \pm 0.015\text{GeV} \qquad m_Z = 91.1876 \pm 0.0021 \qquad [3]$$

Z bosons are responsible for weak neutral currents that conserve the quark and lepton number (also called flavour). While the lepton number is always conserved independently for each generation in the SM the quark flavour can be changed by charged currents mediated with W bosons that couple up-type quarks with down-type quarks. Mixing between the quark generations is described by the CKM matrix. The weak interaction violates parity (P)- the processes are not invariant under a sign flip of the spacial coordinates. This is manifested in the fact that the weak interaction couples only to the left-handed chiral projections of the fermions. In the limit of vanishing particle masses the left-handed chiral states correspond to the left-handed helicity states (spin points in opposite direction to the momentum). This causes all neutrinos to be (helicity) left-handed and all antineutrinos to be right-handed. The corresponding processes also violate charge conjugation (C) symmetry (flip all charge like quantum numbers and make particles to antiparticles). The combined symmetry CP is conserved in first approximation. CP violation has been observed in systems with neutral mesons. Theoretically this is described by introducing complex phases in the CKM matrix. [4]
Although some properties of the gravitational interaction can be described by exchange of spin-2 gravitons [5] no quantum field theory describing gravitation at all energy scales has been found yet. As a consequence the standard model doesn't include gravitation.

Generation	Lepton	Charge [e]	Mass [MeV]
1	e	-1	$0.510998928 \pm 0.000000011$
	ν_e	0	≈ 0
2	μ	-1	$105.6583715 \pm 0.0000035$
	ν_μ	0	≈ 0
3	τ	-1	1776.82 ± 0.16
	ν_τ	0	≈ 0

Table 2.1: Lepton families and observed masses [3]

Generation	Quark	Charge [e]	Mass [MeV]
1	u	$+\frac{2}{3}$	$2.3^{+0.7}_{-0.5}$
	d	$-\frac{1}{3}$	$4.8^{+0.7}_{-0.3}$
2	c	$+\frac{2}{3}$	$(1.275 \pm 0.025) \cdot 10^3$
	s	$-\frac{1}{3}$	95 ± 5
3	t	$+\frac{2}{3}$	$(173.5 \pm 0.6 \pm 0.8) \cdot 10^3$
	b	$-\frac{1}{3}$	$(4.18 \pm 0.03) \cdot 10^3$

Table 2.2: Quark families and observed masses [3]

2.2 Quantum field theory

Quantum field theory allows a relativistic description of quantum mechanics. Everything is described by fields. In contrast to discrete mass points in classical (quantum-) mechanics fields are continuous functions of spacetime. The field's dynamics are defined via a Lagrange density $\mathcal{L}$ (here referred to as "Lagrangian") which is a function of the fields and their derivatives. Classical field equations can be derived from the field theory Euler-Lagrange-Equations. [6]

$$\partial_\mu \left(\frac{\partial \mathcal{L}}{\partial(\partial_\mu \phi)} \right) - \frac{\partial \mathcal{L}}{\partial \phi} = 0 \tag{2.1}$$

Fields that satisfy these equations minimise the action

$$S = \int \mathcal{L} \mathrm{d}^4 x$$

The transition to quantum fields is done using the path integral or the canonical formalism [5]. The resulting integrals can be solved for free fields which are described by Lagrangians that contain only harmonic terms. To describe interactions, anharmonic terms have to be introduced. These are included as perturbative expansions in the coupling parameters. The perturbation series can be represented as Feynman diagrams. They consist of "propagators" which are the amplitude for a particle to propagate and of "vertices" which represent interactions. Propagators are drawn as lines and vertices as intersections between lines. Although the calculation is mostly done in momentum space, the diagrams can be easily interpreted as spacetime diagrams. For the diagrams in this thesis the time axis goes from left to right.
Evaluating the perturbation series includes integration over arbitrary high momenta. Some of these integrals don't converge ("ultraviolet divergence"). The solution is to regularise the integrals e.g. by imposing a "cut-off" energy scale and to "renormalise" several parameters. This leads to the observable fact that several physical quantities like coupling constants depend on the considered energy scale.

2.3 Gauge theories

The fields in the Standard Model have the property to leave the Lagrangian invariant under certain transformations. This means that different mathematical fields describe the same physical quantities - the symmetry reflects a redundancy in the mathematical description [5].
Theories can be constructed out of the desired symmetries. Global symmetries (not spacetime dependent) lead to conserved charges as a consequence of Noether's theorem. To achieve invariance under a local (spacetime dependent) transformation it is necessary to introduce a "gauge field" which transforms in a way that it makes the Lagrangian invariant in total. The SM is based on the abelian U(1) and the non-abelian SU(N) symmetry groups.

2.3.1 U(1)

The free Dirac Lagrangian

$$\mathcal{L} = \bar{\psi}(i\gamma^\mu\partial_\mu)\psi - m\bar{\psi}\psi$$

describes non interacting massive fermions. Invariance under local U(1) transformations

$$\psi(x) \to e^{i\alpha(x)}\psi(x)$$

can be achieved by introducing a gauge field A_μ. This can be done by replacing the derivative ∂_μ by the covariant derivative

$$D_\mu = \partial_\mu + ieA_\mu$$

where A_μ has to transform as

$$A_\mu(x) \to A_\mu(x) - \frac{1}{e}\partial_\mu\alpha(x)$$

The dynamics of the gauge field are described by

$$\mathcal{L} = -\frac{1}{4}F_{\mu\nu}F^{\mu\nu} \tag{2.2}$$

with the field strength tensor

$$F_{\mu\nu} = \partial_\mu A_\nu - \partial_\nu A_\mu$$

Calculating Eq. (2.1) with Eq. (2.2) leads to the Maxwell equations. The full Maxwell-Dirac Lagrangian now reads

$$\mathcal{L} = \bar{\psi}(i\gamma^\mu D_\mu)\psi - \frac{1}{4}F_{\mu\nu}F^{\mu\nu} - m\bar{\psi}\psi$$

It describes Fermions interacting with the electromagnetic field. The theory is called Quantum Electrodynamics (QED). [6]

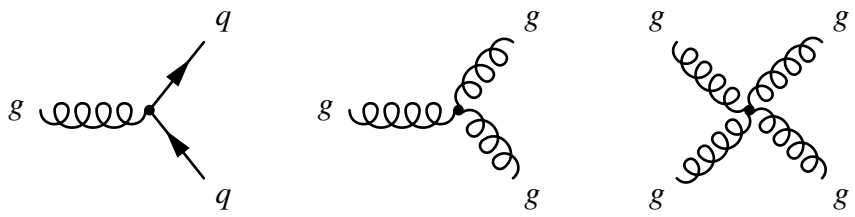

Figure 2.1: Vertices of QCD

2.3.2 SU(N)

The same concept of creating gauge invariant theories has also been developed for SU(N) symmetries (Yang-Mills-Theory). The SU(N) covariant derivative becomes

$$D_\mu = \partial_\mu - igA^a_\mu t^a \qquad a = 1, ..., (N^2 - 1)$$

The t^a are the generators of SU(N). Each generator corresponds to one gauge field being introduced. The field strength tensors are

$$F^a_{\mu\nu} = \partial_\mu A^a_\nu - \partial_\nu A^a_\mu + g f^{abc} A^b_\mu A^c_\nu \tag{2.3}$$

where f^{abc} are the structure constants given by the commutation relation

$$[t^a, t^b] = i f^{abc} t^c$$

The third term in Eq. (2.3) allows quadratic and cubic terms of the gauge fields. They correspond to a self interaction of the gauge bosons in terms of Feynman diagrams. [6]

2.4 The Standard Model as a Gauge theory

The SM is based on invariance under transformations of the symmetry groups $SU(3) \otimes SU(2) \otimes U(1)$.

2.4.1 QCD

The $SU(3)$ symmetry describes the strong interaction. The theory is also called Quantum Chromodynamics (QCD). $SU(3)$ has 8 generators which leads to 8 gauge fields (the gluons) in the QCD Lagrangian. Figure 2.1 shows vertex diagrams corresponding to the interactions of the gluons with quarks and the gluon self interaction.

The strong coupling constant decreases with increasing energy and decreasing length scale, respectively. This makes perturbation theory impossible for low energies - when

the coupling parameter is greater than 1, higher order diagrams contribute more than lower order diagrams. The coupling is predicted to behave like

$$\alpha_s(Q) = \frac{2\pi}{b_0 \log(Q/\Lambda)}$$

where b_0 depends on the number of quarks (6 in the SM) and Λ is the energy scale at which α_s becomes "strong" and perturbation theory breaks down (around 200 MeV from experiments). The fact that the strong interaction becomes weak at small distant scales and so quarks behave like free particles inside hadrons is called "asymptotic freedom".

2.4.2 The Higgs mechanism

Gauge theories always contain massless gauge bosons and introducing mass terms destroys the gauge symmetry. However, the bosons mediating the weak interaction are observed to be very massive. To describe the weak interaction as a gauge theory, a mechanism to generate masses of the gauge bosons is needed. Such a mechanism has been proposed in 3 papers by Brout and Englert, Higgs, Guralnik and Hagen in 1964 [7–9].
The idea is to use a concept called "spontaneous symmetry breaking" in the context of gauge theories. This is done by introducing a scalar field with a non-zero vacuum expectation value (ground state). Spontaneously breaking a continuous symmetry leads to the occurrence of massless "Goldstone bosons". In a gauge theory the degrees of freedom of the scalar field are absorbed as masses for the gauge bosons. Metaphorically: The gauge bosons acquire mass by "eating" the Goldstone bosons. [6]

The Higgs field

The part of the Lagrangian describing the scalar field (Higgs field) ϕ is formulated as

$$\mathcal{L} = |D_\mu \phi|^2 - V(\phi) \tag{2.4}$$

where

$$V(\phi) = -\mu^2 \phi^* \phi + \frac{\lambda}{2}(\phi^* \phi)^2 \tag{2.5}$$

In case of U(1) ϕ is represented as a complex number and $V(\phi)$ can be visualised as a "Mexican hat" (see Figure 2.2). In the ground state the scalar field will "choose" one of the minima of the potential (metaphorically: "roll down the Mexican hat"). The minima occur at

$$\phi^* \phi = \frac{\mu^2}{\lambda} \equiv v^2$$

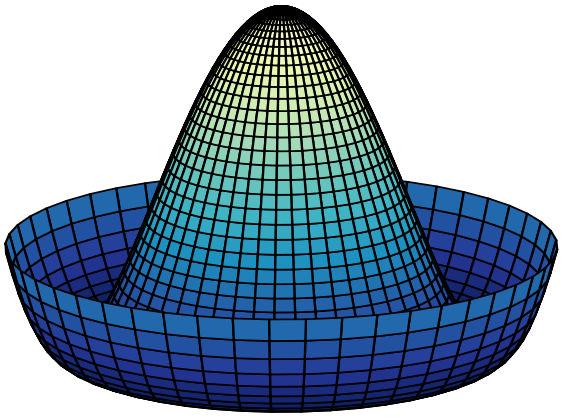

Figure 2.2: “Mexican hat” potential

The Higgs boson

The scalar fields ground state can be expanded in small fluctuations around the vacuum expectation value. In the SU(2) case one can choose to write

$$\phi(x) = \frac{1}{\sqrt{2}} \begin{pmatrix} 0 \\ v + h(x) \end{pmatrix}$$

The potential energy part of Eq. (2.5) becomes

$$\begin{aligned} \mathcal{L} &= -\mu^2 h^2 - \lambda v h^3 - \frac{1}{4}\lambda h^4 \\ &= -\frac{1}{2} m_h^2 h^2 - \sqrt{\frac{\lambda}{2}} m_h h^3 - \frac{1}{4}\lambda h^4 \qquad m_h \equiv \sqrt{2}\mu \end{aligned}$$

which is the Lagrangian of a massive scalar particle with mass m_h referred to as the “Higgs boson”. All particles that couple to the Higgs field also couple to the massive Higgs boson (see Figure 2.3). [6]

2.4.3 Electroweak theory

The electromagnetic and weak interaction in the SM are described by a unified description developed by Glashow, Weinberg and Salam (GWS) [10–12]. The theory is build from $SU(2) \otimes U(1)$ with the covariant derivative

$$D_\mu = \partial_\mu - igA_\mu^a T^a - ig' Y B_\mu \tag{2.6}$$

A_μ^a are the three gauge fields of SU(2), B_μ is the gauge field of U(1). Y is the charge associated with the U(1) symmetry, g and g' are the coupling constants for the SU(2) and U(1) gauge fields. The Pauli matrices are generators of SU(2) so $T^a = \sigma^a/2$ is used here.

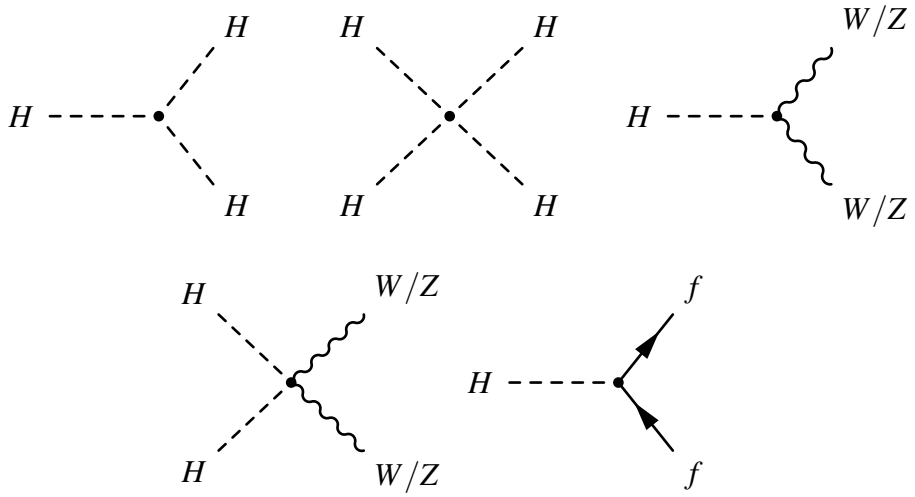

Figure 2.3: SM couplings of the Higgs boson

Massive gauge bosons

The gauge boson acquire mass via one Higgs doublet. The charge Y for the Higgs field is 1/2. The vacuum expectation value can be chosen to have the form

$$\langle \phi \rangle = \frac{1}{\sqrt{2}} \begin{pmatrix} 0 \\ v \end{pmatrix}$$

Using the covariant derivative from Eq. (2.6) in the Higgs field Lagrangian from Eq. (2.4) with this vacuum expectation value gives the three massive vector bosons - identified as the mediators of the weak interaction

$$W_\mu^\pm = \frac{1}{\sqrt{2}}(A_\mu^1 \mp i A_\mu^2) \qquad \text{with} \quad m_W = g\frac{v}{2}$$

$$Z_\mu^0 = \frac{1}{\sqrt{g^2+g'^2}}(gA_\mu^3 - g'B_\mu) \qquad \text{with} \quad m_Z = \sqrt{g^2+g'^2}\frac{v}{2}$$

and one massless boson - identified as the photon (γ)

$$A_\mu = \frac{1}{\sqrt{g^2+g'^2}}(g'A_\mu^3 + gB_\mu)$$

The electric charge can be identified by writing the covariant derivative in terms of the physical bosons $W_\mu^\pm, Z_\mu^0$ and A_μ. It is given by

$$Q = T^3 + Y \tag{2.7}$$

Figure 2.4 shows the vertices corresponding to the interactions of the physical bosons. It is convenient to rewrite the coupling constants g and g' in terms of the electron charge e

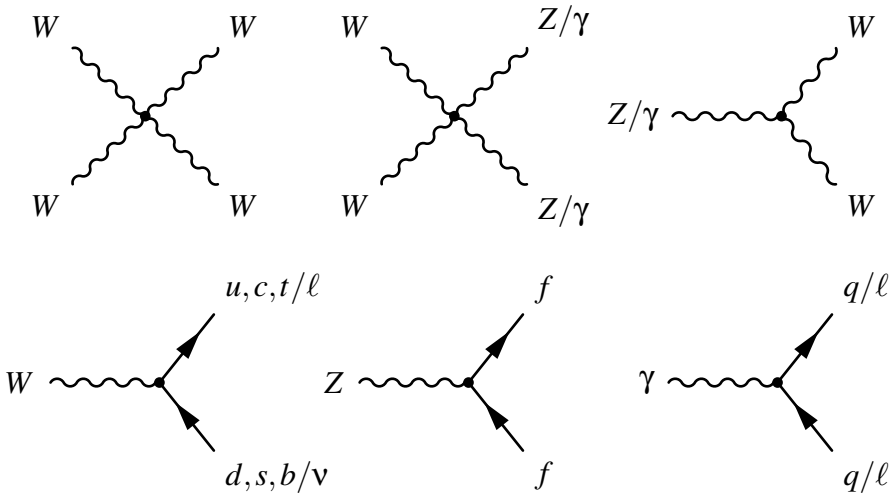

Figure 2.4: Interactions of the Z, W and γ bosons

and the "weak mixing angle" θ_w:

$$\cos\theta_w = \frac{g}{\sqrt{g^2+g'^2}} \qquad \sin\theta_w = \frac{g'}{\sqrt{g^2+g'^2}} \qquad e = \frac{gg'}{\sqrt{g^2+g'^2}}$$

The weak mixing angle defines the change of basis from (A^3, B) to (Z^0, A)

$$\begin{pmatrix} Z^0 \\ A \end{pmatrix} = \begin{pmatrix} \cos\theta_w & -\sin\theta_w \\ \sin\theta_w & \cos\theta_w \end{pmatrix} \begin{pmatrix} A^3 \\ B \end{pmatrix}$$

and relates the W and Z boson mass

$$m_W = m_Z \cos\theta_w.$$

Weak interactions with fermions

The parity violation of the weak interaction is described by writing the left-handed fermion fields as doublets

$$E_L = \begin{pmatrix} \nu_e \\ e^- \end{pmatrix} \qquad Q_L = \begin{pmatrix} u \\ d \end{pmatrix}$$

and making the right-handed fields singlets. The fermion part of the Lagrangian (without masses, only first generation) is

$$\mathcal{L} = \bar{E}_L(i\not{D})E_L + \bar{e}_R(i\not{D})e_R + \bar{Q}_L(i\not{D})Q_L + \bar{u}_R(i\not{D})u_R + \bar{d}_R(i\not{D})d_R \qquad (\not{D} = \gamma^\mu D_\mu) \quad (2.8)$$

The terms for right-handed neutrinos are all zero - in this model all neutrinos are left-handed. Each covariant derivative gets the values for Y assigned in a way that it leads to the desired electric charge according to Eq. (2.7). The charged and neutral current interactions are also given by Eq. (2.8). Figure 2.4 shows the vertices for these interactions. [6]

2.4.4 Fermion masses

Mass terms couple left-handed fermions to right-handed fermions e.g.

$$\mathcal{L} = -m_e(\bar{e}_L e_R + \bar{e}_R e_L)$$

which makes them impossible in the context of the electroweak gauge theory. Fermion mass terms can be generated by introducing a Yukawa coupling to the Higgs field. For Leptons the terms can be written as

$$\mathcal{L}_e = -\lambda_e \bar{E}_L \cdot \phi e_R + h.c.$$

And for quarks

$$\mathcal{L}_q = -\lambda_d \bar{Q}_L \cdot \phi d_R - \lambda_u \varepsilon^{ab} \bar{Q}_{La} \phi_b^\dagger u_R + h.c.$$

When ϕ is replaced by its vacuum expectation value the terms become

$$\mathcal{L}_e = -\frac{1}{\sqrt{2}} \lambda_e v \bar{e}_L e_R + h.c. + \cdots .$$

with the mass $m_e = 1/\sqrt{2}\lambda_e v$ and

$$\mathcal{L}_q = -\frac{1}{\sqrt{2}} \lambda_d v \bar{d}_L d_R - \frac{1}{\sqrt{2}} \lambda_u v \bar{u}_L u_R + h.c. + \cdots .$$

with the masses $m_{u/d} = 1/\sqrt{2}\lambda_{u/d} v$, respectively.
The observable consequence of this mechanism is that fermions can couple to the Higgs boson (see Figure 2.3). The mechanism can be generalised to include the observed quark mixing via the CKM matrix [6].

2.5 SM processes at proton collisions

Many theoretical predictions mentioned in the previous sections can be tested at proton collisions as they occur at the Large Hadron Collider. This section shows a selection of processes that can be investigated, in particular the production and decay of Higgs bosons and the background in the search for a $H \to WW$ decay, with the Higgs boson produced in vector boson fusion.

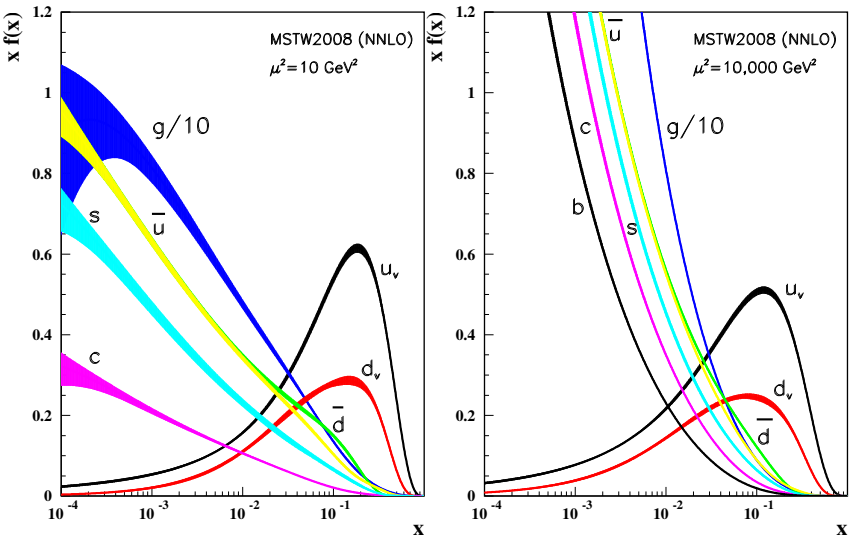

Figure 2.5: Examples for parton distribution functions at scales $\mu^2 = 10\text{GeV}^2$ (left) and $\mu^2 = 10^4\text{GeV}^2$ (right)

2.5.1 Parton distribution functions

Protons are three quark bound states (uud) of the strong interaction mediated by gluons. When colliding protons at high energies inelastic scattering occurs. Then the interactions happen between quarks or gluons ("partons"). Gluons can fluctuate in $q\bar{q}$ pairs, so it is possible to collide other quark flavors than up or down quarks and also antiquarks even without colliding antiprotons. The "original" up and down quarks are called "valence quarks" and tend to collide with larger fractions of the proton momentum as the gluons and the quarks from $q\bar{q}$ splitting ("sea quarks").
In a reference frame where the protons are moving rapidly toward each other ("infinite momentum frame") the constituents move collinear with the momentum to the proton. In this frame the inelastic scattering of protons is described by the parton distribution functions (PDFs). The PDFs describe the density distribution of a certain parton that carries a fraction x of the proton momentum. The distribution functions depend on x and the momentum transfer Q^2. Perturbative QCD cannot predict the PDFs but when measured for a given scale it is possible to extrapolate to other scales [6]. Figure 2.5 shows PDFs for 2 different scales. At small momentum fractions the interactions are dominated by gluons. The knowledge of the PDFs is crucial to be able to calculate cross sections at pp collisions.

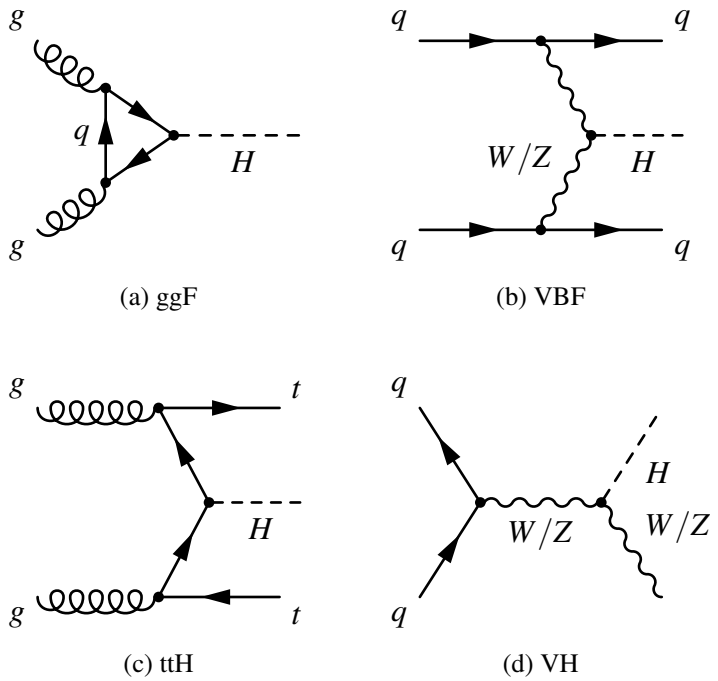

(a) ggF (b) VBF

(c) ttH (d) VH

Figure 2.6: Example diagrams for dominant Higgs boson production modes at pp collisions

2.5.2 Higgs boson production

The dominant process to produce a Higgs boson in pp collisions is the gluon-gluon fusion (ggF), followed by the vector-boson fusion (VBF), the production in association with a (W or Z) vector boson (VH) and the $t\bar{t}$ associated production (ttH) (see Figure 2.6). Although the gluon-gluon fusion process has the largest cross section (see Figure 2.7) the other production modes offer some additional particles in the final state, that can be a distinctive signature against the background.
In this thesis the VBF production mode is investigated. The final state contains two quarks that can be identified as jets in the detector ("tagging jets"). The jets have high momenta and tend to lie close to the beam axis. Since the Higgs boson production is entirely electroweak, jet production in the central region between the tag jets is strongly suppressed [13]. This helps to distinguish against background events where the jets originate from gluon radiation which fills a much larger phase space.

2.5.3 Higgs boson decay

Since the Higgs mechanism in the SM is responsible for all particle masses the Higgs boson is expected to be able to decay (at tree level) into all particles that carry a mass.

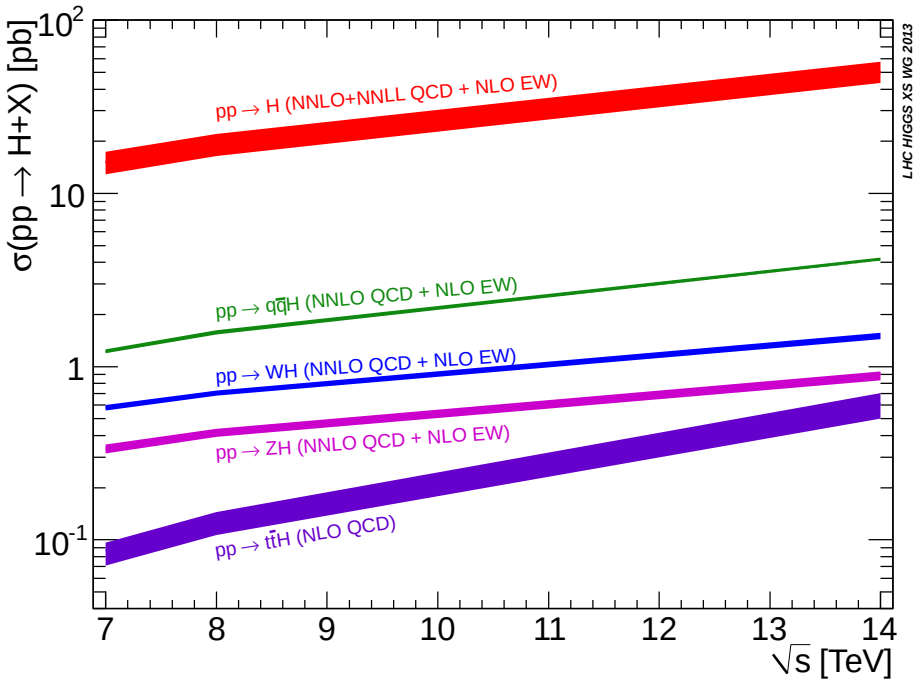

Figure 2.7: Higgs boson production cross sections at pp collisions for a Higgs boson with a mass of 125 GeV recommended by the LHC Higgs cross section working group [14,15].

In addition, there are higher order decay modes like $\gamma\gamma$, gg, $Z\gamma$ where the leading order contributions come from top quark or W boson loops. Figure 2.8 shows the Higgs boson branching ratios for a Higgs boson mass around 125 GeV where the ATLAS and CMS Collaboration observed a particle consistent with the SM Higgs Boson [16, 17].
In this mass range the decay into WW or ZZ is suppressed because the bosons are off mass shell ("virtual"). The dominant decay into b quark pairs is challenging due to the large background from QCD production. The most sensitive channels are $\gamma\gamma$ and ZZ where a signal has been observed both for ATLAS and CMS. For WW [18, 19] and $\tau\tau$ [20, 21] there is currently (August 2014) evidence at a level of 3-4 standard deviations.
In this thesis the decay into WW with leptonically decaying W bosons ($H \to WW \to \ell^+\nu\ell^-\bar{\nu}$) is analysed (Figure 2.9). For the leptons electrons and muons are considered. In the following leptons denoted as "ℓ" are either electrons or muons. Tau leptons are denoted as "τ". There are also neutrinos in the final state which are not reconstructed in the detector. They leave missing transverse energy ($\not{E}_T$) as a signature.
A distinctive feature of this decay comes from spin correlations. The Higgs boson is a scalar (spin 0) particle. Therefore, the W (spin 1) bosons have their spins pointing in opposite direction. In the Higgs boson rest frame the W bosons also have their momenta pointing in opposite direction. Since the weak interaction couples only to left handed particles this causes the neutrino to be emitted in opposite direction of the W^+ boson spin

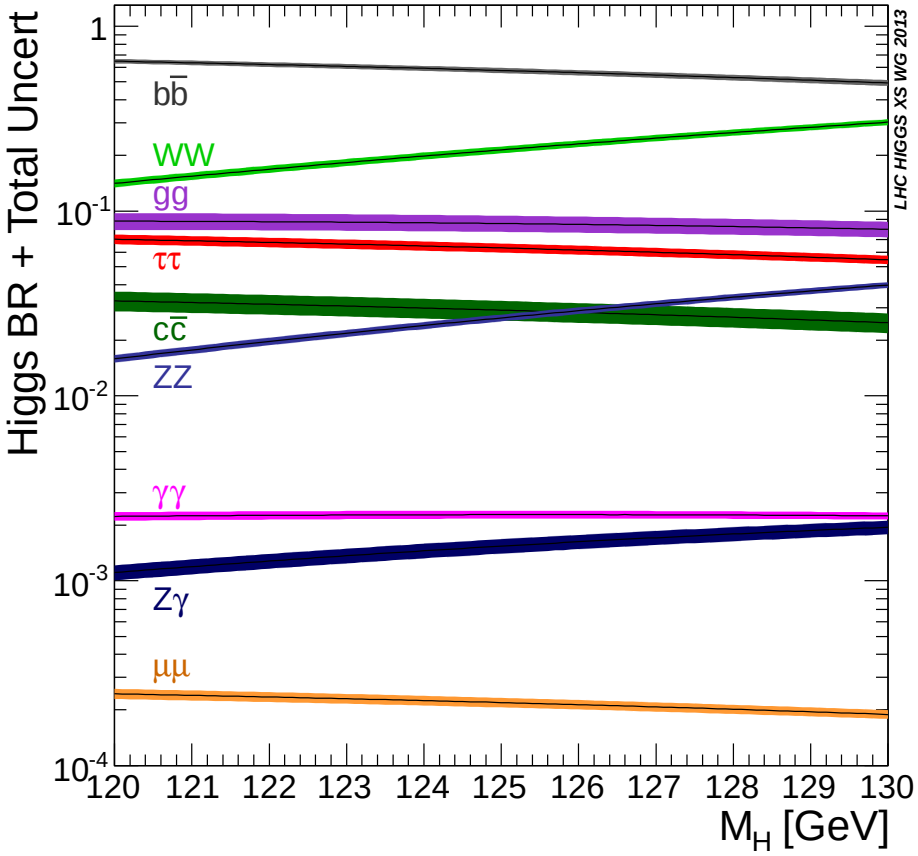

Figure 2.8: Higgs boson branching ratios recommended by the LHC Higgs cross section working group [14, 15]

and the antineutrino in direction of the W^- boson spin. In total the neutrinos tend to go in opposite direction to the charged leptons which can be observed by a tendency to small opening angles between the lepton tracks and small invariant mass of the dilepton system (see Figure 2.10).

2.5.4 Backgrounds of VBF $H \to WW \to \ell^+\nu\ell^-\bar{\nu}$

The possibility to use the characteristics of the tagging jets allows a better separation between signal and background for the VBF production mode (compared to ggF). The most challenging backgrounds are the top quark pair production ($t\bar{t}$), the dilepton production via Z/γ exchange (Z+jets) and the direct production of 2 W bosons (WW).

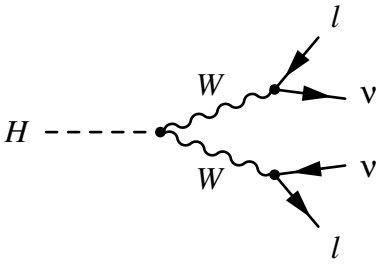

Figure 2.9: Higgs boson decay into WW that decay leptonically

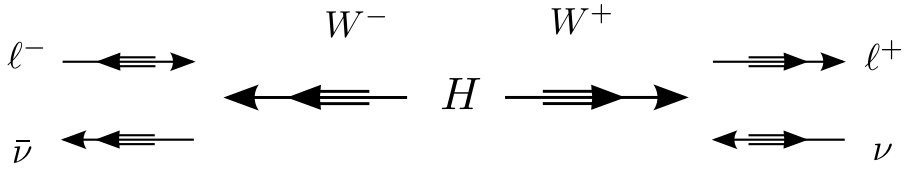

Figure 2.10: Spin correlations in $H \to WW \to \ell^+\nu\ell^-\bar{\nu}$. The single line arrow indicates the momentum direction, the double line arrow points in the direction of the spin.

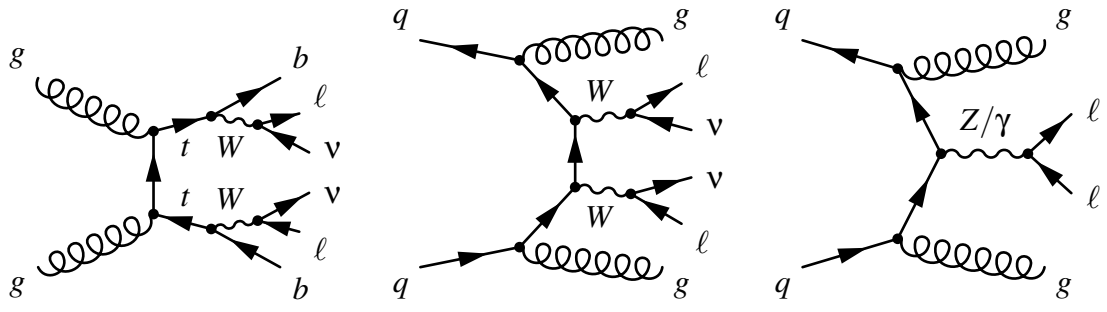

(a) $t\bar{t}$ (b) WW+2 jets (c) Z+2 jets

Figure 2.11: Example diagrams for the three main backgrounds in the VBF $H \to WW$ analysis

$t\bar{t}$

The $t\bar{t}$ process (Figure 2.11a) has an intrinsically similar topology to the VBF $H \to WW$. The top quarks decay weakly via radiation of W bosons into 2 bottom quarks which are visible as 2 jets in the detector. A significant reduction of this dominant background is only possible via identification of b quark jets (b tagging). In addition to $t\bar{t}$ there is a smaller background contribution from single top quark production.

Z+jets

The Z/γ production at proton collisions is dominated by the Drell Yan process (Figure 2.11c). Although there are no neutrinos in the dileptonic final states, this process has a large cross section and becomes a relevant background via fake $\not{E}_T$ from energy resolution effects. Z+jets is the dominant background after all selections for the final states with 2 same flavour leptons (ee, $\mu\mu$). In the opposite flavour final states ($e\mu$) it is less dominant as it enters almost exclusively via leptonic decays of τ-leptons from $Z \to \tau\tau$.

WW

The partly irreducible W boson pair production (Figure 2.11b) gives the smallest contribution of the top 3 backgrounds in the VBF channel. It has a smaller cross section than Z+jets and is further suppressed by the jet requirements.

Subdominant backgrounds

Smaller contributions come from diboson production other than WW and from single W production with additional jets (W+jets) and QCD multijet production. The W+jets and QCD background enter via jets that are misidentified as ("fake") leptons. The ggF Higgs boson production is also taken as a background in this analysis.

Chapter 3

Experimental setup

This chapter gives a summary of the Large Hadron Collider and the ATLAS Experiment. In this thesis ATLAS data from proton proton collisions is used.

3.1 LHC

The Large Hadron Collider is a 27 km long hadron-hadron ring collider located at CERN near Geneva. It is capable of colliding protons and also heavy ions. The hadrons are accelerated in opposite direction in two separate beam pipes sharing the same confinement tube. The tube is installed underground in the tunnel that was previously used for the Large Electron Positron Collider (LEP). The particles are accelerated in 8 straight sections and bent in 8 arcs by superconducting magnets. The goal for proton-proton collisions is a centre of mass collision energy of $\sqrt{s}$=14 TeV. This requires a peak dipole magnetic field of 8.33 T in the arc sections to keep the beams in the circular path. Nominally the beams are organised in 2808 bunches of approx. 10^{11} protons with a bunch spacing of 25 ns. The acceleration is achieved by superconducting radio frequency (RF) cavities in the straight sections.
The potential frequency f_{event} of a certain event is given by the luminosity L and the cross section σ_{event} of the event

$$f_{event} = \sigma_{event} L$$

The LHC aims to achieve a peak luminosity of $10^{34}\text{cm}^{-2}\text{s}^{-1}$ [22]. The inelastic proton-proton cross-section is about 80 mb, so there are 10^9 inelastic events/s expected at peak luminosity. This corresponds to 23 interactions per bunch crossing [23].
There are beam crossing points at four of the straight sections in the Octants 1,2,4,8 where the caverns for the ATLAS, ALICE, LHCB and the CMS experiment are located. Before the protons enter the LHC they pass an injection chain of former CERN accelerators that have been upgraded for the needs of the LHC (see Figure 3.1) [22].

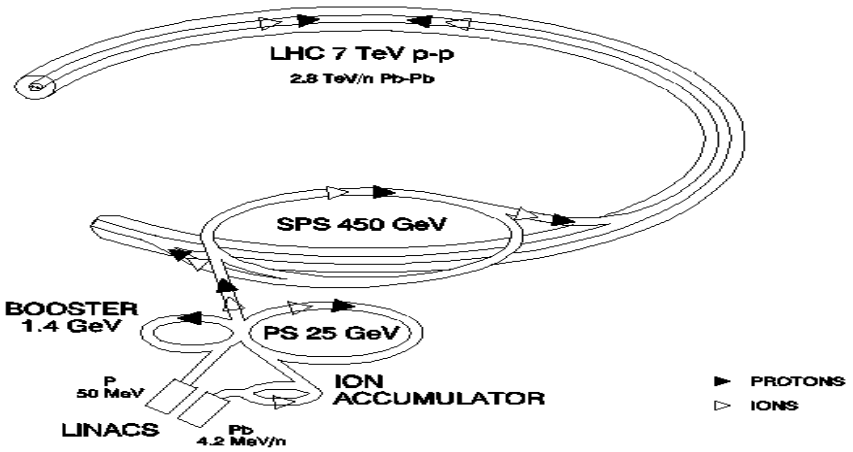

Figure 3.1: The LHC injection chain [22]

3.2 ATLAS

The ATLAS (A Toroidal LHC ApparatuS) detector is one of the two high luminosity experiments at the LHC. The detector has a size of 44m in length and 25m in height. It consists of several layers of different types of detectors that cover almost the full solid angle. The combination of all detector systems allows particle identification and measurement of particle momenta (tracking) and energy deposits (calorimetry). The different types of detectors are arranged in several layers of cylindrical barrel parts for the central region and end cap disks for the forward and backward region (Figure 3.2). A detailed description of the ATLAS detector is given in [23].

3.2.1 Coordinate System

The detector's coordinate system has the origin at the interaction point. The z-axis points in direction of the beam. The positive x-axis points in direction of the centre of the LHC ring and the positive y-axis is pointing upwards. The azimuthal angle ϕ is measured in the x-y (transverse) plane, the polar angle θ is the angle from the beam axis. The rapidity y and the pseudorapidity η (see Figure 3.3) are defined as

$$y = \frac{1}{2}\ln\frac{E+p_z}{E-p_z} \qquad \eta = -\ln\tan\frac{\theta}{2}$$

where E is the energy of the object whose rapidity is calculated and p_z its momentum in z-direction. Differences in rapidity are invariant under boosts in the z-direction and for

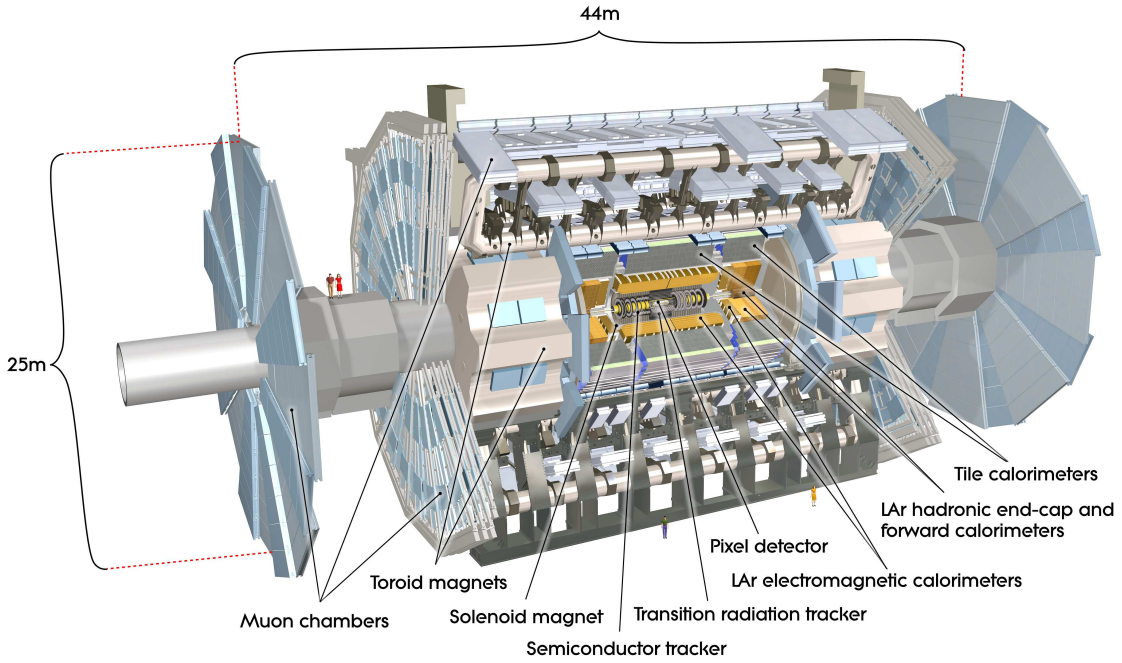

Figure 3.2: Layout of the ATLAS detector

$p \gg m$ the rapidity is approximated by the pseudorapidity [3]. The distance ΔR in the $\phi - \eta$ plane is defined as

$$\Delta R = \sqrt{\Delta\eta^2 + \Delta\phi^2} \tag{3.1}$$

3.2.2 Inner Detector

The purpose of the inner detector is the precise measurement of charged particle tracks. It consists of an innermost layer of silicon pixel detectors followed by a layer of silicon microstrip (SCT) trackers and a straw tube based Transition Radiation Tracker (TRT). The pixel detector and the SCTs provide the best position resolution: 10 μm (R-ϕ) and 115 μm (z) for the pixel detectors and 17 μm (R-ϕ) and 580 μm (z) for the SCTs. The high accuracy close to the interaction point is important for reconstruction of the impact parameter and second vertices which is needed for heavy-flavour and τ-lepton tagging. The TRT has the capability to detect the particle track (R-ϕ) with an accuracy of 130 μm per straw tube. In addition, it can detect transition radiation photons for electron identification. The inner detector is embedded in a 2 T solenoidal magnetic field. This allows the determination of the particle's charge and momentum by measuring the bending of the track.

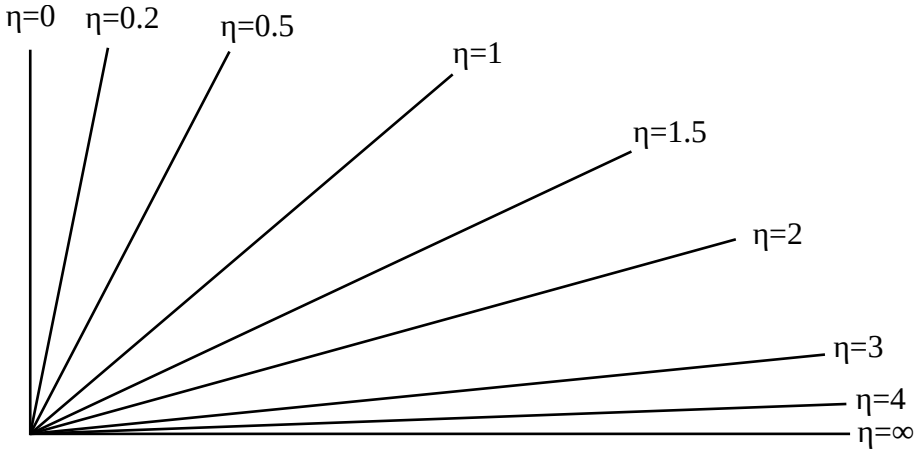

Figure 3.3: Angles corresponding to several values of the pseudorapidity η

3.2.3 Calorimeters

The inner detector is surrounded by a system of calorimeters. Ideally the calorimeters should absorb all electromagnetic and hadronic particle showers and measure the total deposited energy. This is achieved with alternating layers of absorption and active material ("sampling calorimeters"). The barrel part of the Calorimeter consists of the accordion shaped electromagnetic (EM) calorimeter with lead absorber and liquid Argon (LAr) as active material and a hadronic calorimeter with steel absorber and scintillating tiles (tile calorimeter). The end caps consist of a electromagnetic calorimeter with a similar technique like the barrel EM calorimeter and a copper-LAr hadronic end cap. The end cap area close to the beam axis is surrounded by the LAr forward calorimeter (FCal) which consists of a EM calorimeter with copper absorber and two hadronic calorimeters with mainly tungsten as absorber material. The LAr in the FCal is filled in a gap between rods and tubes parallel to the beam axis. The performance goals for the energy resolution of the calorimeters, given as $\frac{\Delta E}{E} = a/\sqrt{E} \oplus b$ are $10\%/\sqrt{E} \oplus 0.7\%$ for the EM calorimeter, $50\%/\sqrt{E} \oplus 3\%$ for the hadronic calorimeter and $100\%/\sqrt{E} \oplus 10\%$ for the forward calorimeter. The performance goals were verified using test beams.

3.2.4 Muon system

The muon system is the outermost part of the detector. The barrel part is embedded in a toroidal magnetic field that bends the muon tracks to allow charge and momentum determination. The magnetic field in the barrel part is generated by 8 large air-core coils. In addition, there are two smaller systems of 8 coils in the end caps that are shifted by 22.5° with respect to the barrel toroid system. The end cap muon detectors are arranged in front and behind the end cap toroid coils.

Precision measurement of muon tracks is achieved by several layers of optically aligned "Monitored" Drift Tube chambers (MDTs). The first layer of the end caps in front of the toroids consists of Cathode Strip Chambers (CSCs) which are multiwire proportional chambers that are suitable for the high counting rates in this region. The outer end caps are large wheels with MDTs. The achieved resolution is 60 μm per CSC plane and 80 μm per MDT tube layer.
The precision chambers are supported by a trigger system of Resistive Plate Chambers (RPCs) in the barrel and Thin Gap Chambers (TGCs) in the end caps. In addition to their capability of triggering the storage of events they provide orthogonal coordinate measurement to the precision chambers.

3.2.5 Forward detectors

There are three other detectors at a larger distance from the interaction point. Two of them mainly measure the luminosity provided for ATLAS: LUCID (LUminosity measurement using Cerenkov Integrating Detector) is installed 17m from the interaction point and ALFA (Absolute Luminosity For ATLAS) at 240m. LUCID measures the inelastic, ALFA the elastic p-p scattering at small angles. The third one is the Zero-Degree Calorimeter (ZDC) which is installed at 140m and detects forward neutrons in heavy-ion collisions.

3.2.6 Trigger system

The 25 ns bunch spacing creates a 40 MHz event rate. To bring this rate down to a storable amount each event has to pass a chain of three trigger systems. The L1 trigger selects events with high transverse momentum particles using the information from the muon trigger chambers and reduced granularity information from the calorimeters and brings the event rate down to 75 kHz. It builds up Regions of Interest (RoI) which are passed to the L2 trigger. The L2 trigger uses full detector information in the RoI accepting events at a rate of around 3.5 kHz. The final stage is the event filter which uses the full events and brings the rate down to 200 Hz for long term storage. Each event has a storage size of approximately 1.3 Mbyte.

3.2.7 Data taking in 2011 and 2012

The first long proton-proton run of the LHC started in 2011 with a centre of mass energy ($\sqrt{s}$) of 7 TeV. It was followed by a $\sqrt{s} = 8$ TeV run in 2012. Both runs operated with a bunch spacing of 50 ns [24]. ATLAS recorded a (time-) integrated luminosity of 5.08 fb^{-1} in 2011 and 21.3 fb^{-1} in 2012 (Figure 3.4). At the moment (2014) the LHC is shut down for maintenance. The next run is planned to start in 2015 with $\sqrt{s} = 13$ TeV. The analysis of this thesis uses the $\sqrt{s} = 7$ TeV ATLAS data recorded in 2011.

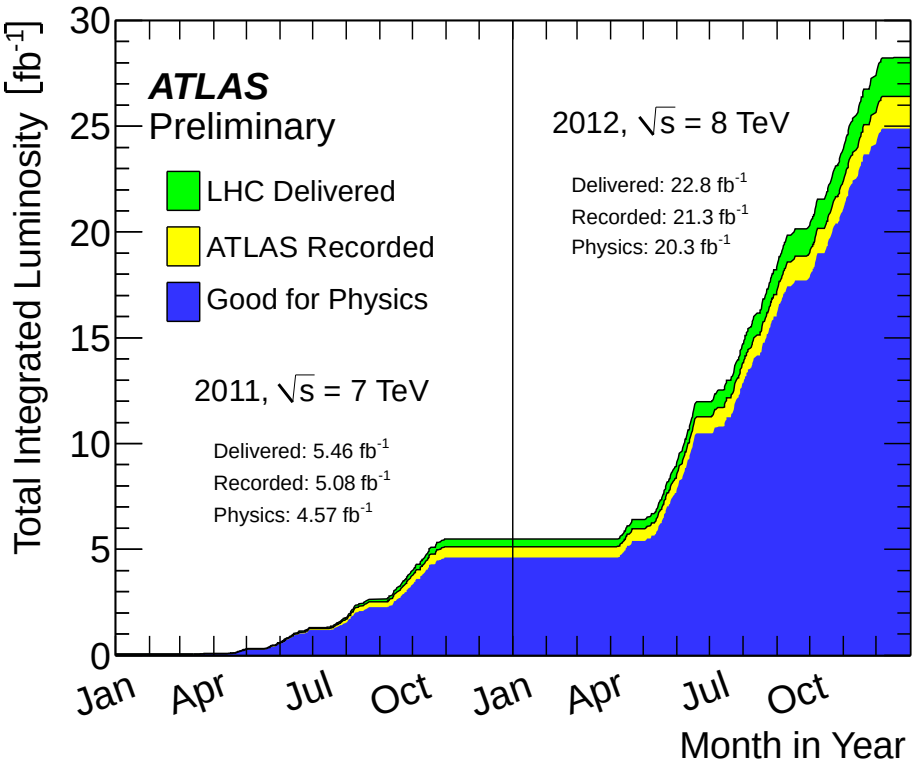

Figure 3.4: Luminosity recorded by ATLAS in 2011 and 2012 [25]

Chapter 4

Analysis of $H \rightarrow WW$ decays in VBF production

This chapter describes the analysis of $H \rightarrow WW$ decays in VBF production with 7 TeV ATLAS data using a cut based approach. This means the signal/background ratio is enhanced by selecting only events which fulfil lower or upper bounds on several one-dimensional physical observables. The analysis is derived from the cut based 8 TeV VBF analysis described in [26]. The goal is to apply optimisations from the 8 TeV analysis to the 7 TeV data set (as much as possible) in order to simplify the combination.
The baseline approach for the VBF $H \rightarrow WW$ channel is a multivariate analysis based on boosted decision trees (BDT) which has been shown to give the best performance in this channel. To support and cross check the BDT analysis the additional cut based analysis is performed.

4.1 Data and Monte Carlo samples

After applying the "Good-Run-List" criteria which reject events where relevant detector components were not working properly an integrated luminosity of $4.5\,\text{fb}^{-1}$ is left. Events from single lepton triggers are the starting point of the selection. Depending on the luminosity period different triggers were available. For the first period a $p_{\text{T}} > 20\,\text{GeV}$ electron trigger with "medium" operating point is used (`e20_medium`). For the higher luminosity period $p_{\text{T}} > 22\,\text{GeV}$ was available (`e22_medium`) and for the highest luminosity an additional veto on energy in the hadronic calorimeters behind the electron cluster is introduced ("vh"), together with re-optimised electron identification (`e22vh_medium1`) [27]. For muons $p_{\text{T}} > 18\,\text{GeV}$ threshold triggers are used (`mu18` for the beginning and `mu18_medium` for the higher luminosity periods) [28].

To study the distributions of observables for the signal and the backgrounds and to estimate the expected number of events after certain selections Monte Carlo (MC) simulation data is used (for corrections from data see section 4.3). The simulated number of events is scaled to the measured integrated luminosity using the predicted total cross section of the process. The statistical uncertainty on the MC prediction is given by a Poisson distribution which can be approximated by a Gaussian distribution with standard deviation $\sqrt{N}$ for large N. The total statistical uncertainty on the number of predicted events becomes

$$\sigma_{\mathrm{MC,stat}} = \frac{\sqrt{N_{\mathrm{sim}}}}{N_{\mathrm{sim}}} \times N_{\mathrm{scaled}} \tag{4.1}$$

where N_{sim} is the number of simulated events that pass a certain selection and N_{scaled} is the expected number of events that pass the selection, given by the simulated number scaled to the integrated luminosity and predicted cross section.
The MC generation is done in several steps. Event generators use theoretical predictions from perturbation theory matrix elements to generate the "hard process" and extend the event by additional radiation of particles that were not included in the matrix element calculation. The additional radiation (e.g. "parton shower" QCD radiation) and hadronisation of quarks and gluons can in general only be simulated using approximations. The detector response is then simulated either by a full simulation of the ATLAS detector using GEANT4 [29] or by a fast simulation where CPU time consuming calorimeter shower simulations are replaced by presimulated showers or a parametrisation of the detector response. All MC samples used for this analysis use the full simulation, except for the s- and t-channel single top samples that use the ATLFAST-II [30] simulation program.
The hard process of most samples is simulated using POWHEG [31], a next to leading order (NLO) event generator. It can be interfaced with showering generators like PYTHIA6 [32], PYTHIA8 [33] or HERWIG [34]. Table 4.1 summarises the generators for the MC samples used in this analysis.

4.2 Event selection

4.2.1 Object selection

The selection of leptons, jets and the calculation of the main observables is done in a dedicated stage of the analysis. In this stage small ntuples are created that contain only the necessary information (mainly the observables described in the next section) to perform the event selection. This analysis uses ntuples that are produced from 7 TeV ATLAS data with the same lepton and jet selection as for the analysis presented at the 48th Rencontres de Moriond in 2013 (described in [18]).

Process	Generator
ggF Higgs	POWHEG+PYTHIA8 [33]
VBF Higgs	POWHEG+PYTHIA8
WH/ZH	PYTHIA6
$qq \to WW$	POWHEG+PYTHIA6
$gg \to WW$	GG2WW [35]
Z/γ^* +jets	ALPGEN [36] + HERWIG [34]
Z/γ^* +jets (electroweak)	SHERPA [37]
$W\gamma^*$ ($m_{\ell\ell} > 7$ GeV)	ALPGEN+HERWIG
$W\gamma^*$ ($m_{\ell\ell} < 7$ GeV)	SHERPA
WZ/ZZ	POWHEG
$t\bar{t}$	POWHEG+PYTHIA6
Single top s-channel and Wt-channel	POWHEG+PYTHIA6
Single top t-channel	ACERMC [38] + PYTHIA6

Table 4.1: MC samples used in this analysis

Leptons

For the analysis object selection the electrons have to satisfy a set of tight cut based criteria ("tight++") that use both tracking (including the transition radiation measurement) and calorimeter information. Muons are selected by combining the muon spectrometer and inner detector information by a statistical combination ("STACO") procedure. Electrons are allowed in the range $|\eta| < 2.47$ except for the transition region between the barrel and end cap part ($1.37 < |\eta| < 1.52$), muons in the range $|\eta| < 2.5$. To suppress contributions from the fake backgrounds W+jets and QCD the leptons are required to be "isolated". Track transverse momenta or calorimeter deposits within a cone of a certain radius ΔR in the $\eta - \phi$ plane (see Eq. 3.1) around the object's track are required to be only a small fraction of the lepton momentum and energy, respectively. In addition, the lepton tracks have to originate from the primary vertex which is ensured by requirements on the track's impact parameter. A track's impact parameter is the closest distance between the track and the reconstructed primary vertex. Table 4.2 shows the isolation and impact parameter requirements. EtConeXX is the sum of the transverse energies in calorimeter cells within a cone of radius $\Delta R = 0.XX$ around the object's track, PtConeXX is the sum of the track transverse momenta within that cone.

$$\text{EtCone}XX = \sum_{\text{cells, } \Delta R(\text{object track,cell}) < 0.XX} E_{\text{T,cell}}$$

$$\text{PtCone}XX = \sum_{\text{tracks, } \Delta R(\text{object track,track}) < 0.XX} p_{\text{T,track}}$$

Electrons	Muons
$p_{\mathrm{T}}^{\mathrm{sublead}} > 15\,\mathrm{GeV}$:	
$D_0^{\mathrm{sig}} < 10$	$D_0^{\mathrm{sig}} < 3$
$\lvert Z_0 \rvert < 1\,\mathrm{mm}$	$\lvert Z_0 \sin\theta \rvert < 1\,\mathrm{mm}$
EtConeCor30/$p_{\mathrm{T}} < 0.12$	EtConeCor30/$p_{\mathrm{T}} < \min(0.20, 0.0125 p_{\mathrm{T}} - 0.14)$
PtCone40/$p_{\mathrm{T}} < 0.06$	PtCone30/$p_{\mathrm{T}} < \min(0.15, 0.011 p_{\mathrm{T}} - 0.12)$
$p_{\mathrm{T}}^{\mathrm{sublead}} < 15\,\mathrm{GeV}$:	
same	$D_0^{\mathrm{sig}} < 1.5$
same	same
EtConeCor30/$p_{\mathrm{T}} < 0.05$	same
PtCone40/$p_{\mathrm{T}} < 0.08$	PtCone40/$p_{\mathrm{T}} < 0.05$

Table 4.2: Impact parameter and isolation requirements for electrons and muons

For EtconeXX the core of the cone around the object, corresponding to 5x7 cells, is removed from the sum. A pileup correction is applied for EtconeXX (EtConeCorXX). The impact parameter requirements are given in terms of the transverse impact parameter significance D_0^{sig}, which is the transverse impact parameter divided by its estimated uncertainty, and the longitudinal impact parameter Z_0. At least one lepton candidate must match a trigger object. The data is split into 4 categories of the the identified flavour of the leading and subleading p_{T} lepton: $e\mu$, μe, ee, $\mu\mu$. The analysis is performed in two channels: "different flavour" ($e\mu/\mu e$) and "same flavour" ($ee/\mu\mu$).

Jets

Jets are reconstructed using the anti-k_T algorithm [39] with the radius parameter R=0.4. Furthermore, the jet vertex fraction (JVF) has to be greater than 0.75. The JVF is a discriminant that reflects the fraction of tracks, associated to the jet, that originate from the primary vertex. Jets are accepted in the region $|\eta| < 4.5$. The tagging jet p_{T} thresholds are $p_{\mathrm{T}} > 25\,\mathrm{GeV}$ for $|\eta| < 2.5$ and $p_{\mathrm{T}} > 30\,\mathrm{GeV}$ for $|\eta| > 2.5$. Figure 4.2 (left) shows the distribution of the tag jets. The VBF signal is found at most in the 2 jet bin.

B tagged jets

To discriminate the VBF signal against the top background it is necessary to identify jets which originate from b quarks. B quarks form b hadrons which have long enough life

times that the distance they travel before decaying can be seen as a secondary vertex in the detector. The MV1 [40] algorithm combines this with other kinematic properties of b-jets into a single discriminant using neural networks. In this analysis the MV1 discriminant is cut at 85% b-tagging efficiency. The p_{T} threshold for the b jets is chosen to be 20 GeV (slightly lower than for the tag jets). Figure 4.2 (right) shows the distribution of the number of b tagged jets. The top background is concentrated in the bins with b tagged jets.

Missing transverse energy

At hadron collisions the total energy of the final state particles of all interactions is unknown as a significant fraction escapes in the beam pipe. However, the momenta balance in the transverse plane. The quantity that represents escaped energy in the transverse plane (e.g. from neutrinos) is the missing transverse energy. In this analysis this quantity is important to discriminate against the Z+jets background where no neutrinos are present and to calculate observables that make use of the expected presence of neutrinos. Two definitions of missing transverse energy are used. "$\not{E}_T$" is calculated from calorimeter energies and muon tracks, "$\not{E}_{\mathrm{T}}^{\mathrm{track}}$" is calculated from track momenta with the track momenta associated to jets being replaced by their calorimeter energy.

4.2.2 Observables

The signal in terms of the VBF production mode is mainly characterised by the properties of the 2 leading jets in the final state. The $H \to WW \to \ell\nu\ell\nu$ decay leaves a signature in terms of properties of the leptons and the missing transverse energy. There are also some quantities that combine the lepton, jet and $\not{E}_T$ properties.

- m_{jj}:
  The invariant mass of the dijet system
- ΔY_{jj}:
  The rapidity difference of the dijet system
- $p_{\mathrm{T}}^{\mathrm{tot}} = |\mathbf{p}_{\mathrm{T}}^{\ell 1} + \mathbf{p}_{\mathrm{T}}^{\ell 2} + \not{\mathbf{E}}_{\mathrm{T}}^{\mathrm{track}} + \sum \mathbf{p}_{\mathrm{T}}^{\mathrm{jets}}|$:
  The magnitude of the (vector-) sum of transverse momenta of leptons, (all reconstructed) jets and $\not{\mathbf{E}}_{\mathrm{T}}^{\mathrm{track}}$
- $p_{\mathrm{T}}^{\mathrm{lead}}$, $p_{\mathrm{T}}^{\mathrm{sublead}}$:
  the transverse momentum of the leading and subleading lepton
- $m_{\ell\ell}$:
  The invariant mass of the dilepton system

- $\Delta\phi_{\ell\ell}$:
  The azimuthal opening angle between the leptons

- $m_{\mathrm{T}} = \sqrt{(E_{\mathrm{T}}^{\ell\ell} + \not{E}_{\mathrm{T}}^{\mathrm{track}})^2 - (\mathbf{p}_{\mathrm{T}}^{\ell\ell} + \not{\mathbf{E}}_{\mathrm{T}}^{\mathrm{track}})^2}$:
  The transverse mass of the dilepton system and $\not{E}_{\mathrm{T}}^{\mathrm{track}}$. $E_{\mathrm{T}}^{\ell\ell}$ is the sum of the energies of both leptons and $\mathbf{p}_{\mathrm{T}}^{\ell\ell}$ is the sum of their (3-) momentum vectors.

- $m_{\tau\tau}$:
  This variable estimates the hypothetical ditau invariant mass. It is calculated using the collinear approximation method. The leptons are assumed to be coming from leptonically decaying taus. Furthermore, the $\not{E}_{\mathrm{T}}^{\mathrm{track}}$ is assumed to come only from neutrinos of τ decays and the neutrinos are assumed to be collinear with the observed leptons (e, μ). From this the fractions of $\not{E}_{\mathrm{T}}^{\mathrm{track}}$ that are carried by each neutrino can be calculated. If the equations yield a physical result (positive energy fractions) then the hypothetical invariant mass of the ditau system is calculated (otherwise the event passes the requirement on this variable).

4.2.3 Signal region

A series of requirements on several observables define a region that is enhanced in the VBF $H \to WW$ process. Monte Carlo distributions for the signal and background processes are shown in figures 4.3-4.7. The signal distribution in plots with linear y-axis is scaled to have approximately the same integral as the total background. For all plots, except the $\not{E}_T$ distribution and the number of jets, the preselection, the b-jet veto and the Z veto were applied. If not stated otherwise $e\mu/\mu e$ and $ee/\mu\mu$ are combined. A dashed red line in the plots indicates the value where the cut is applied. The impact of the selection criteria on the background composition is visualised in figure 4.1.

Preselection

The following selection represents rough criteria that characterise the final state that is searched for.

- exactly two leptons (e or μ) with opposite sign of the electric charge
- high energetic leptons: $p_{\mathrm{T}}^{\mathrm{lead}} > 22$ GeV, $p_{\mathrm{T}}^{\mathrm{sublead}} > 10$ GeV
- dilepton invariant mass above Υ-meson ($b\bar{b}$) resonances:
  $m_{\ell\ell} > 10$ (12) GeV for $e\mu/\mu e$ ($ee/\mu\mu$)
- at least two jets

Background suppression

Some cuts are specifically designed to suppress certain backgrounds:

- leave out the region dominated by Z decays ("Z-Veto"):
  $|m_{\ell\ell} - m_Z| > 15$ GeV (for $ee/\mu\mu$)
- $\not{E}_T > 45\,\text{GeV}$ is applied for the $ee/\mu\mu$ channel to suppress the Z+jets background further. For $e\mu/\mu e$ all major backgrounds (including the Z+jets contamination from $Z \to \tau\tau$) also create real $\not{E}_T$ from neutrinos, so no cut is applied here (see figure 4.3).
- $m_{\tau\tau} < (m_Z - 25\text{ GeV})$ ($Z \to \tau\tau$ Veto): This suppresses parts of the $Z \to \tau\tau$ background and helps to avoid overlap with the $H \to \tau\tau$ analysis (see figure 4.4).
- $p_{\mathrm{T}}^{\mathrm{tot}} < 15\,\text{GeV}$:
  In the ideal case events without hadronic radiation, which is not identified as jets, should have $p_{\mathrm{T}}^{\mathrm{tot}} = 0$ as the transverse momenta of the leptons, jets and neutrinos ($\not{E}_T$) balance. Significant $p_{\mathrm{T}}^{\mathrm{tot}}$ represents soft hadronic momentum (not identified as jets) that recoils against the lepton+jet system. The upper bound suppresses the contamination with the fake backgrounds W+jets and QCD and in general events with soft QCD radiation (see figure 4.4).
- no b-tagged jets (b-Veto):
  This reduces significantly the top background

VBF topology

The following criteria enhance the signal fraction by exploiting the properties of the VBF production mode.

- $m_{jj} > 500\,\text{GeV}$ and $\Delta Y_{jj} > 2.8$:
  the VBF tagging jets are expected to lie close to the beam axis and have high momentum (see figure 4.5).
- Central Jet Veto (CJV):
  There is no "colour flow" between the tagging jets, since the Higgs boson production is purely electroweak. Hadronic activity is suppressed in the central region. This is used by rejecting events with additional $p_{\mathrm{T}} > 20\,\text{GeV}$ jets in the rapidity gap of the tagging jets.
- Outside lepton Veto (OLV):
  The charged leptons have to lie inside the rapidity gap of the tagging jets.

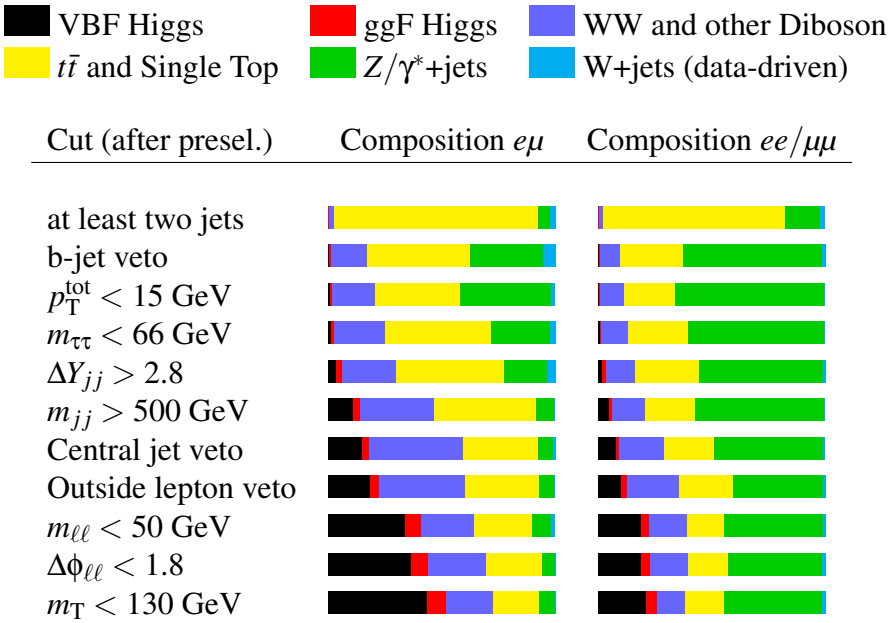

Figure 4.1: Graphical representation of the composition of processes at different cut stages. For the numbers see tables 4.7 - 4.10

$H \to WW \to \ell\nu\ell\nu$ topology

Finally events have to fulfil criteria to enhance the signal characterised by the Higgs decay topology.

- $\Delta\phi_{\ell\ell} < 1.8$ and $m_{\ell\ell} < 50$ GeV:
  Due to spin correlations (see section 2.5.3) the opening angle between the leptons and the invariant mass of the dilepton system are expected to be small (see figure 4.6).

- $m_T <$130 GeV and $m_T >$ 80 GeV for $p_T^{sublead}$ <15 GeV:
  In contrast to the 8 TeV analysis no fit on the transverse mass distribution is performed because of the limited statistics in the 7 TeV data set. Instead, a cut on m_T is applied. The transverse mass distribution is expected to have a steep tail at the Higgs boson mass - motivating the upper bound of 130 GeV. The low m_T region is expected to be more dominated by Z+jets, especially for low $p_T^{sublead}$- motivating the lower bound in this case (see figure 4.7).

Cut	**7 TeV**	8 TeV	Moriond 2013
$\not\!\!E_T$ (for $ee/\mu\mu$)	$>$ **45 GeV**	$>$ 55 GeV	$>$ 45 GeV
$\not\!\!E_{\mathrm{T}}^{\mathrm{track}}$	-	$>$ 50 GeV	-
N_{jets}	≥ 2		
$N_{\mathrm{b-jet}}$	$= 0$		
$m_{\ell\ell}$	$<$ 50 GeV		$<$ 60 GeV
$\Delta\phi_{\ell\ell}$	$<$ 1.8		
$p_{\mathrm{T}}^{\mathrm{tot}}$	$p_{\mathrm{T}}^{\mathrm{tot}} <$ 15 GeV		$p_{\mathrm{T}}^{\mathrm{tot}} <$ 45 GeV
m_{jj}	$>$ **500 GeV**	$>$ 600 GeV	$>$ 500 GeV
ΔY_{jj}	$>$ **2.8**	$>$ 3.6	$>$ 2.8
CJV	applied		
OLV	applied		
$Z \to \tau\tau$ Veto	$m_{\tau\tau} < (m_Z - 25)$ GeV		$\lvert m_Z - m_{\tau\tau}\rvert > 25$ GeV

Table 4.3: Comparison between the event selection in this analysis (7 TeV), the 8 TeV cut-based analysis and the analysis presented at the Moriond conferences 2013

4.2.4 Loosened cuts

The cuts described in the previous section were chosen to be as close as possible to the 8 TeV cut based analysis. This simplifies the combination of the 7 TeV and 8 TeV results and makes it possible to adopt theoretical uncertainties that were derived with 8 TeV Monte Carlo simulation. Due to limited statistics both in the available simulation samples and in the data some cuts had to be loosened. The dijet selections on m_{jj} and ΔY_{jj} have been loosened to the values used for the analysis presented at the Moriond conferences in 2013 [18]. This ensures the 7 TeV top control region (described in the next section) to be populated with data. With the tight $\not\!\!E_T$ requirements from the 8 TeV analysis no simulated event for the Z+jets process survived the final selection. To avoid this the $\not\!\!E_T$ cut has been loosened to 45 GeV and an additional cut on $\not\!\!E_{\mathrm{T}}^{\mathrm{track}}$ is not applied. The loosened $\not\!\!E_T$ cut can also be justified by the lower pileup in the 7 TeV run which results in less fake $\not\!\!E_T$ and hence a lower peaking $\not\!\!E_T$ for Z+jets. Table 4.3 summarises the differences between the cut values of the analysis presented here (7 TeV), the current 8 TeV cut based analysis and the analysis presented at the Moriond conferences 2013.

4.2.5 Blinding

When performing and optimising an analysis there is the danger of creating a bias from knowing what the result will be. In order to avoid a bias as much as possible and still being able to check the consistency of an analysis several techniques of "blinding" are used [41]. In an analysis like the one described here the region where a signal is expected is known in advance. A common method to avoid biased optimisations in this case is to cut out the observed data in this region (or a slightly larger region). Evaluation of simulated data and development of corrections based on measured data is only done in control regions that have a orthogonal selection to the blinded region. The data is not "unblinded" before selection and background estimation techniques are fixed. For the analysis in this thesis events passing all of the following criteria have been removed in the observed data set:

- preselection (see section 4.2.3)
- b-Veto, Z-Veto
- $m_{jj} > 500\,\text{GeV}$ and $\Delta Y_{jj} > 2.8$
- $\Delta\phi_{\ell\ell} < 1.8$ and $m_{\ell\ell} < 50\,\text{GeV}$
- $m_{\text{T}} < 150\,\text{GeV}$

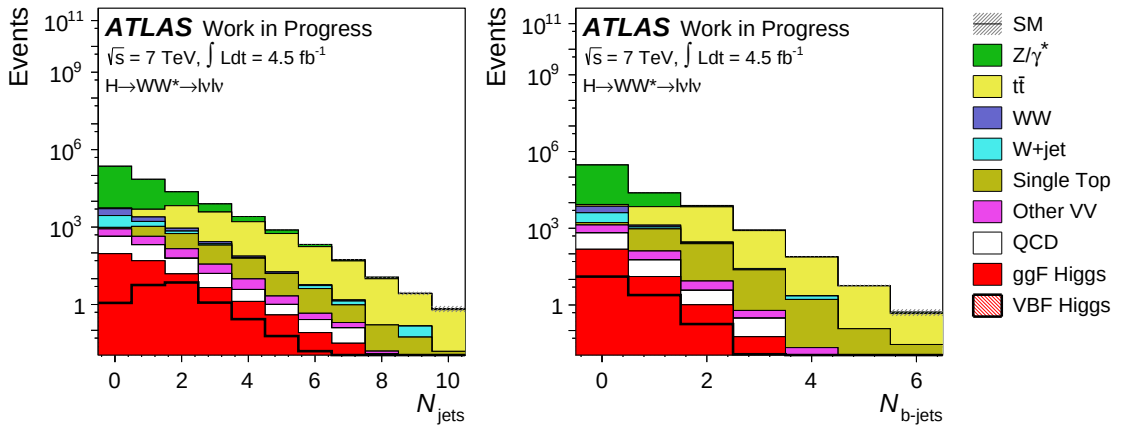

Figure 4.2: The distribution for the number of jets (left) and the number of b-tagged jets (right) after the Z-Veto (no b-jet veto applied)

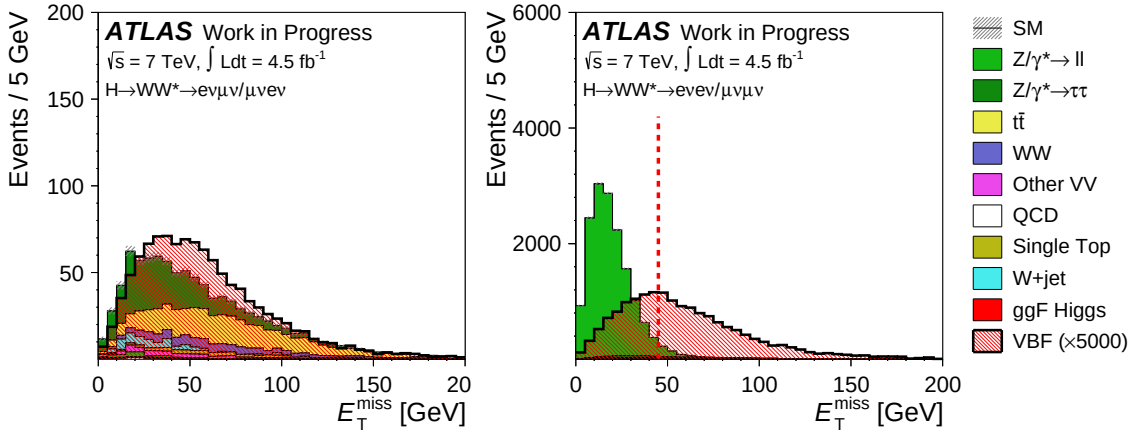

Figure 4.3: The $\not{E}_T$ distribution for $e\mu/\mu e$ (left) and $ee/\mu\mu$ (right).

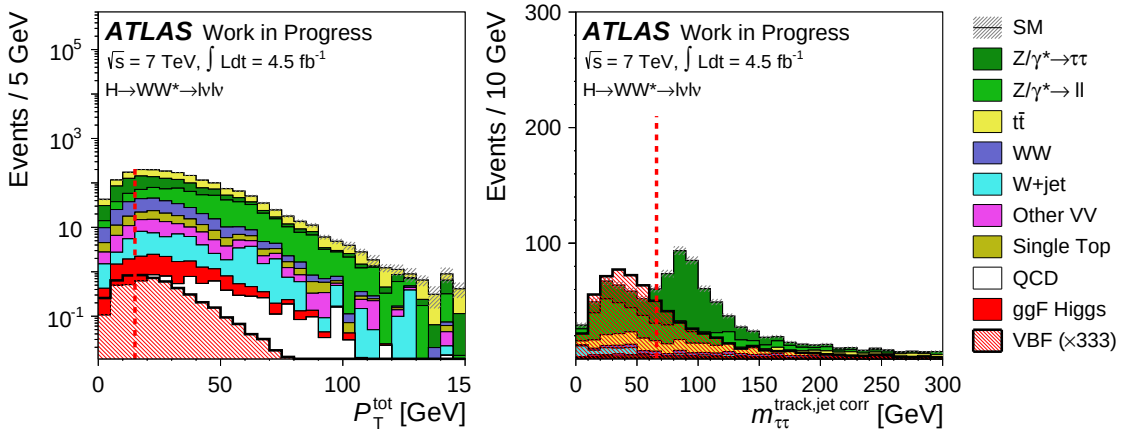

Figure 4.4: The $p_{\mathrm{T}}^{\mathrm{tot}}$ (left) and $m_{\tau\tau}$ (right) distribution.

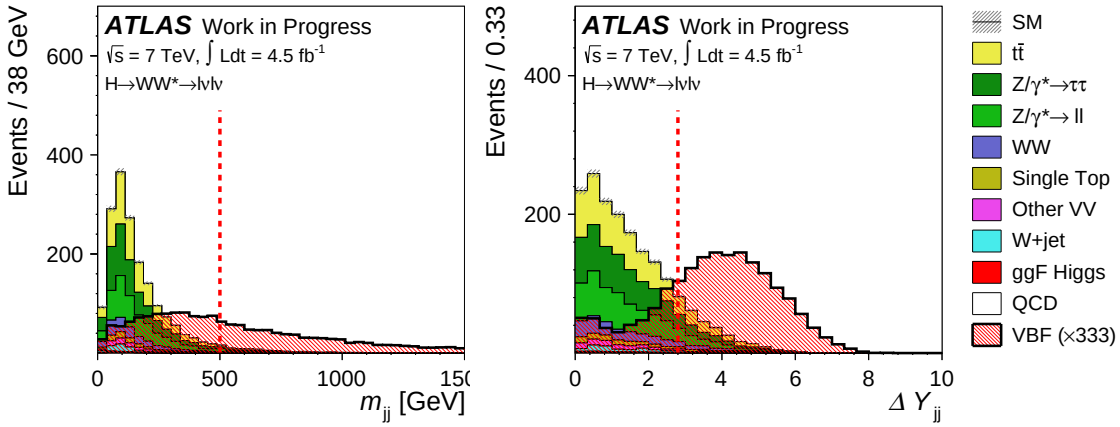

Figure 4.5: The m_{jj} (left) and ΔY_{jj} (right) distribution.

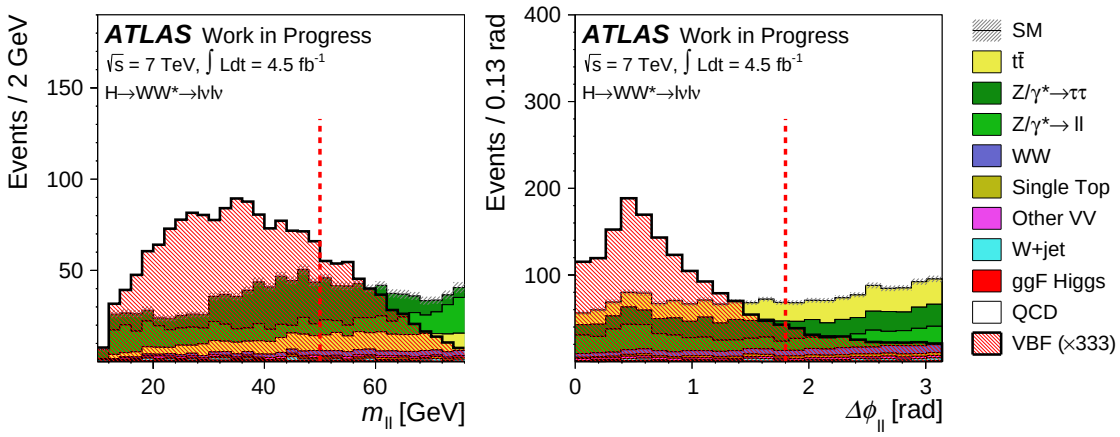

Figure 4.6: The $m_{\ell\ell}$ (left) and $\Delta\phi_{\ell\ell}$ (right) distribution.

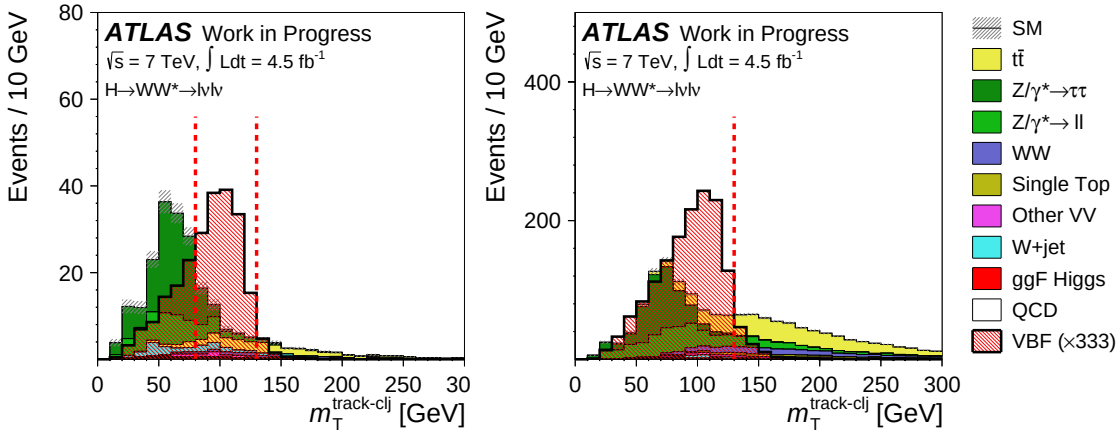

Figure 4.7: The m_{T} distribution for $p_{\mathrm{T}}^{\mathrm{sublead}} < 15\,\mathrm{GeV}$ (left) and $p_{\mathrm{T}}^{\mathrm{sublead}} > 15\,\mathrm{GeV}$ (right).

4.3 Background estimation

In order to be not fully dependent on the predictions of Monte Carlo (MC) simulation the most contributing backgrounds are corrected from data in control regions (CR). The control regions have orthogonal selection to the final signal region (SR) and are constructed to be enriched in the desired process. The "purity" of a control region is the fraction of events of the desired process in the region. A lower purity means more contamination from other backgrounds. Here this procedure is used for the top and the Z+jets background. The W+jets and QCD background is estimated by a purely data-driven technique.

4.3.1 Top

A region enriched in the top background is found by requiring b tagged jets. The purity is 88%. To be as close as possible to the signal region events with exactly one b tagged jet are selected. The control region uses the same preselection as the signal region. In addition the $p_{\mathrm{T}}^{\mathrm{tot}}$ requirement, the $Z \to \tau\tau$-Veto and the VBF topology cuts are applied. Figure 4.8 shows the m_{jj} and ΔY_{jj} distribution before the cut on these variables is applied. The top MC prediction in the signal region is multiplied by a normalisation factor (NF) derived from the top control region. It is defined as the ratio of the number of observed events with the non-top contribution subtracted to the number of top events from MC:

$$NF_{\mathrm{top}} = \frac{N_{\mathrm{data}} - N_{\mathrm{non-top,MC}}}{N_{\mathrm{top,MC}}}$$

The NFs are calculated in a region with the $e\mu/\mu e$ and $ee/\mu\mu$ channel combined and also applied for both channels. Table 4.4 shows the NFs at different cut stages. Within the statistical uncertainty they are close to 1.

Cut	Normalisation factor
Preselection	1.026 ± 0.018
$p_{\mathrm{T}}^{\mathrm{tot}}$	1.087 ± 0.025
$Z \to \tau\tau$-Veto	1.082 ± 0.030
ΔY_{jj}	1.142 ± 0.090
m_{jj}	0.98 ± 0.17
CJV	1.19 ± 0.31
OLV	1.30 ± 0.43

Table 4.4: Normalisation factors in the top control region calculated at different cut stages

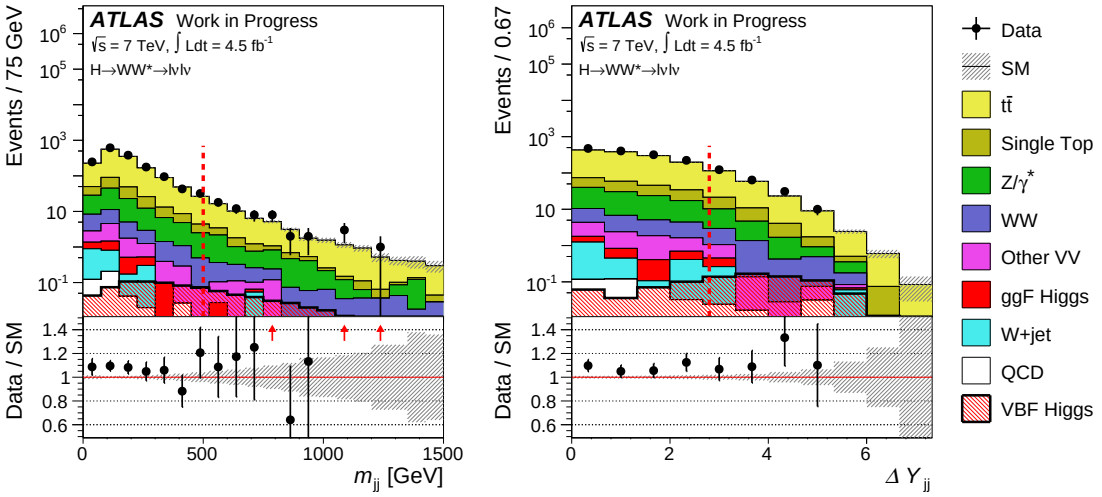

Figure 4.8: The m_{jj} (left) and ΔY_{jj} (right) distribution in the top control region. The $e\mu/\mu e$ and $ee/\mu\mu$ channels are combined. The dashed red line indicates the lower bound where the cut is applied

4.3.2 $Z/\gamma^* \to ee/\mu\mu$ +jets

In the $ee/\mu\mu$ channel the dominant background comes from $Z/\gamma^* \to ee/\mu\mu$ +jets. Control regions can be defined by reverting the $\not{E}_T$ cut or the Z-Veto. The observables $\not{E}_T$ and $m_{\ell\ell}$ which separate the signal region and the control region show mismodelling (figure 4.10). To correct for this a "ABCD" method is used. Four regions (called A,B,C,D) can be defined by splitting the $\not{E}_T$- $m_{\ell\ell}$ plane (see Figure 4.9). Region A is the signal region. With the assumption that $\frac{N_A}{N_B} = \frac{N_C}{N_D}$ ($\not{E}_T$ and $m_{\ell\ell}$ uncorrelated) the number of events in the signal region A can be calculated from the number of events in the control regions B,C,D. In this case the Z+jets MC in region A can be normalised to the data prediction from the ABCD method using

$$\mathrm{NF}_{ABCD,\,\mathrm{simple}} = \frac{B_{\mathrm{data}} \frac{C_{\mathrm{data}}}{D_{\mathrm{data}}}}{A_{\mathrm{MC}}}$$

where X_{data} is the number of data events in region X with the non-Z+jets MC subtracted and X_{MC} the number of MC events in region X. A correlation between $\not{E}_T$ and $m_{\ell\ell}$ can be expressed in terms of a closure factor

$$f_{\mathrm{corr}} = \frac{A/C}{B/D}$$

$Z/\gamma^* \to ee/\mu\mu$		$Z/\gamma^* \to \tau\tau$	
NF_{ABCD}	1.12 ± 0.23	$\mathrm{NF}_{Z\to\tau\tau}$	1.04 ± 0.12
CF_{ABCD}	1.15 ± 0.18	$\mathrm{CF}_{\mathrm{Z-peak}}$	1.44 ± 0.08
$\mathrm{NF}_{ee/\mu\mu}$	$\mathbf{1.29 \pm 0.33}$	$\mathrm{NF}_{e\mu/\mu e}$	$\mathbf{1.49 \pm 0.19}$
f_{corr}	0.61 ± 0.10		

Table 4.5: Composition of the Z+jets normalisation factors NF_{ee+mm}, NF_{em+me} and ABCD non-closure f_{corr}. The errors on the normalisation factors are the statistical uncertainties

With the assumption that f_{corr} is the same when calculated from data as when calculated from MC a corrected normalisation factor can be derived:

$$\mathrm{NF}_{ABCD} = \frac{B_{\mathrm{data}}\frac{C_{\mathrm{data}}}{D_{\mathrm{data}}}}{B_{\mathrm{MC}}\frac{C_{\mathrm{MC}}}{D_{\mathrm{MC}}}} = f_{\mathrm{corr}} \times \mathrm{NF}_{ABCD,\,\mathrm{simple}}$$

It is calculated using the data and MC in the regions B,C,D. To implement the ABCD method in the likelihood fit (see section 4.6) the NF can be rewritten as

$$\mathrm{NF}_{ABCD} = \frac{B_{\mathrm{data}}\frac{C_{\mathrm{data}}}{D_{\mathrm{data}}}}{B_{\mathrm{MC}}\frac{C_{\mathrm{MC}}}{D_{\mathrm{MC}}}} = \mathrm{NF}_C\frac{\mathrm{NF}_B}{\mathrm{NF}_D} = \mathrm{NF}_C \times \mathrm{Ratio}_{BD} \quad \text{with} \quad \mathrm{NF}_X = \frac{X_{\mathrm{data}}}{X_{\mathrm{MC}}}$$

The value for Ratio_{BD} is determined by normalising Region B with $\mathrm{Ratio}_{BD} \times \mathrm{NF}_D$ (see table 4.15). The closure f_{corr} is calculated from MC. Its deviation from 1 ("non-closure") which is 39% in this analysis is used as a systematic uncertainty for the ABCD method. Figure 4.10 shows the $m_{\ell\ell}$ and $\not{E}_T$ distribution before the split into ABCD. The selection before the split is as follows:

- preselection, b-jet veto
- $p_{\mathrm{T}}^{\mathrm{tot}}$ cut (same as SR)
- $Z \to \tau\tau$ Veto
- m_{jj} cut (same as SR)

The statistics in the high $\not{E}_T$ region B is insufficient to apply all the VBF topology cuts on them. To correct for mismodelling of those observables the remaining cuts (ΔY_{jj}, CJV, OLV) are applied in the low $\not{E}_T$, low $m_{\ell\ell}$ region C (figure 4.11). A correction factor (CF) is derived from the ratio of the cut efficiency in non-Z+jets subtracted data and MC:

$$CF = \frac{N_{\mathrm{data,\,cuts}}/N_{\mathrm{data}}}{N_{\mathrm{MC,\,cuts}}/N_{\mathrm{MC}}}$$

low $\not{E}_T$, low $m_{\ell\ell}$			Z-peak (in $m_{\ell\ell}$)		
Presel.	$\rightarrow$ b-Veto	0.963 ± 0.009	Presel.	$\rightarrow$ b-Veto	0.946 ± 0.003
	$\rightarrow p_{\mathrm{T}}^{\mathrm{tot}}$	0.949 ± 0.013		$\rightarrow p_{\mathrm{T}}^{\mathrm{tot}}$	0.930 ± 0.004
	$\rightarrow \Delta Y_{jj}$	1.37 ± 0.19	$p_{\mathrm{T}}^{\mathrm{tot}}$	$\rightarrow \Delta Y_{jj}$	1.423 ± 0.054
	$\rightarrow m_{jj}$	1.32 ± 0.16		$\rightarrow m_{jj}$	1.346 ± 0.046
	$\rightarrow$ CJV	1.56 ± 0.26		$\rightarrow$ CJV	1.490 ± 0.070
	$\rightarrow$ OLV	1.52 ± 0.30		$\rightarrow$ OLV	1.437 ± 0.080

Table 4.6: Evolution of the cut efficiency correction factors for the low $\not{E}_T$ and the Z-peak region

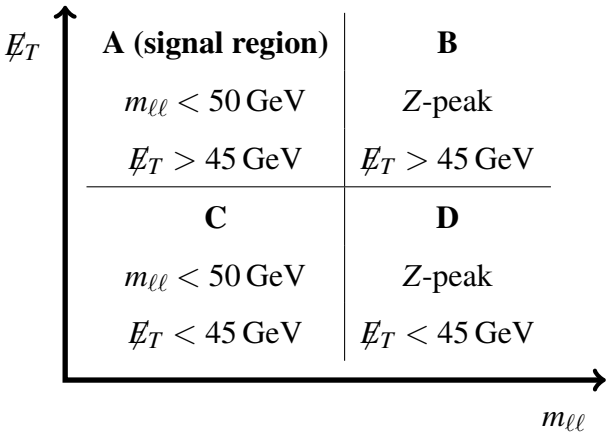

Figure 4.9: Definitions for the ABCD regions

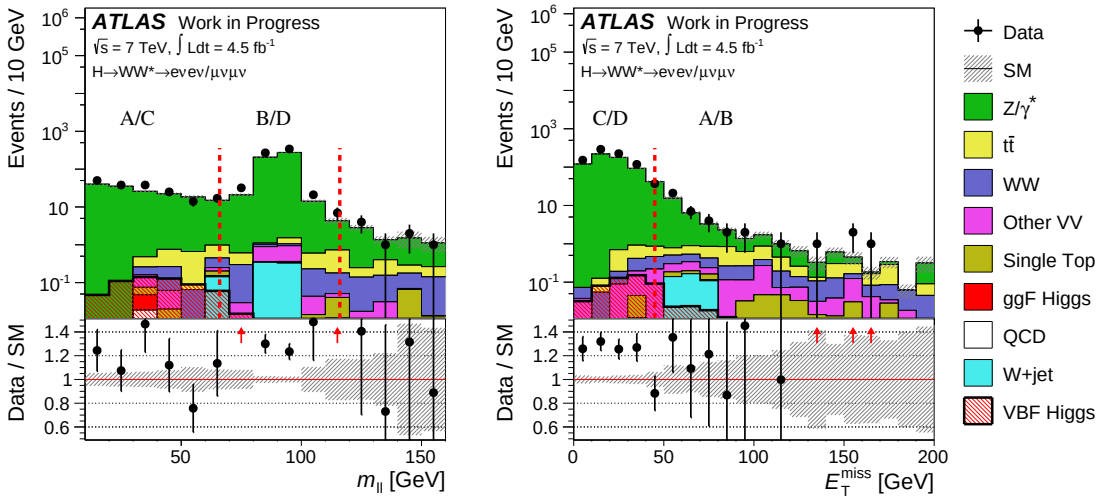

Figure 4.10: The $m_{\ell\ell}$ (left) and $\not{E}_T$ (right) distribution in the region that is split into ABCD.

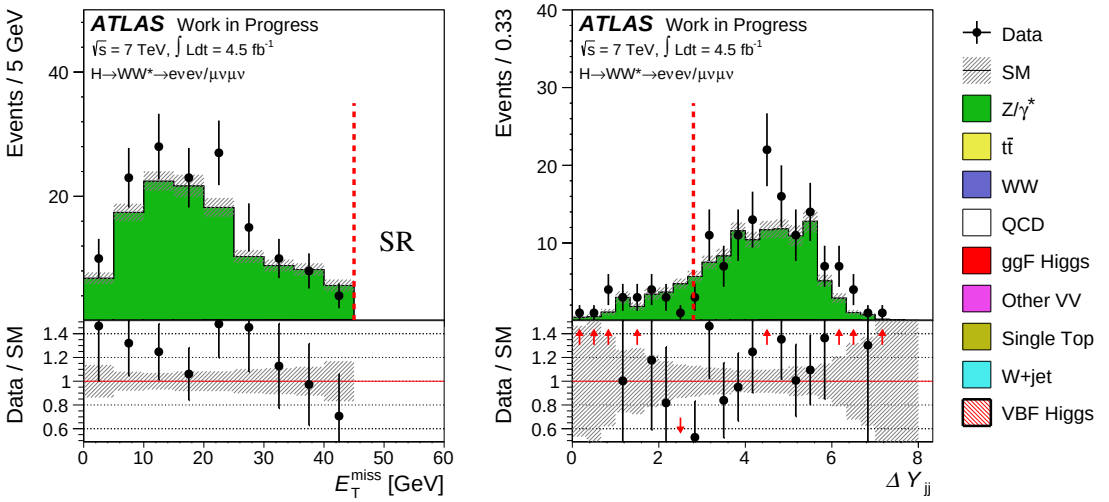

Figure 4.11: The $\not{E}_T$ (left) and ΔY_{jj} (right) distribution in the low $\not{E}_T$, low $m_{\ell\ell}$ region C. The dashed red line in the left plot indicates the separation to the signal region, in the right plot the lower bound where the cut for cut efficiency correction is applied

The ABCD NF, the cut efficiency correction, the resulting total NF and the non-closure f_{corr} are listed in table 4.5. The evolution of the cut efficiency correction factors during the cutflow is shown in table 4.6.

4.3.3 $Z/\gamma^* \to \tau\tau$ +jets

The $Z \to \tau\tau$ MC (which is the main contribution to Z+jets in the $e\mu/\mu e$ channel) is normalised using a $m_{\tau\tau}$ Z-peak region (figure 4.12) with the same NF calculation as for the Top Background. The purity is 90%. The control region is defined by the following cuts:

- preselection, b-jet veto
- $m_{\ell\ell} < 80\,\text{GeV}$
- $p_{\text{T}}^{\text{tot}}$ cut (same as in SR)
- $|m_{\tau\tau} - m_Z| < 25\,\text{GeV}$

Similar to the procedure for $Z/\gamma^* \to ee/\mu\mu$ a correction factor for the VBF topology cuts is calculated. The modelling of jet observables is assumed to be the same for $Z/\gamma^* \to \tau\tau$ and $Z/\gamma^* \to ee/\mu\mu$. The correction is therefore derived from the $ee/\mu\mu$ Z-peak region. The Z-peak region is over 99% pure in the $Z/\gamma^* \to ee/\mu\mu$ process. The low $\not{E}_T$ region is not used here since there is no $\not{E}_T$ cut in the $e\mu/\mu e$ channel. The Z-peak region shows

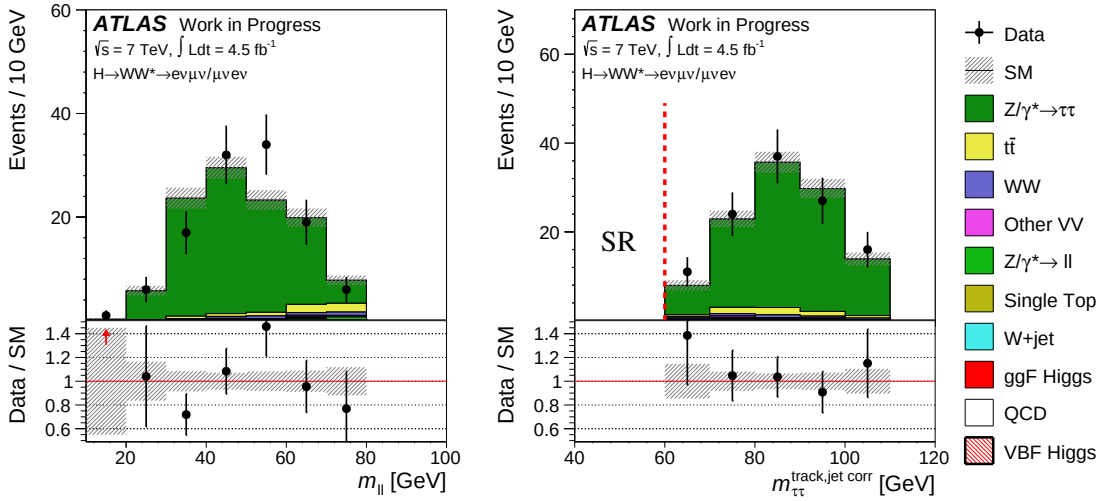

Figure 4.12: The $m_{\ell\ell}$ (left) and $m_{\tau\tau}$ (right) distribution in the $Z/\gamma^* \to \tau\tau$ control region. The dashed red line indicates the separation to the signal region

substantial mismodelling (figure 4.13) in the dijet variables m_{jj} and ΔY_{jj} which leads to a large correction factor. No other than the ALPGEN generated samples were available for the 7 TeV MC, so no systematic uncertainty on this could be derived. The results only have a small dependence on the normalisation of the $Z \to \tau\tau$ background since the $Z \to \tau\tau$ contribution is only 9% in the $e\mu/\mu e$ and 12% in the $ee/\mu\mu$ channel (see tables 4.9 and 4.10) with a MC stat. uncertainty of 71% and 50%. For non-τ $Z \to \ell\ell$ the discrepancy that is seen by comparing the ALPGEN MC with data is covered by the 39% uncertainty on the ABCD method. The right column of table 4.5 shows the normalisation factors for the $Z \to \tau\tau$ MC. The evolution of the cut efficiency correction factors during the cutflow is shown in table 4.6.

4.3.4 W+jets and QCD

W+jets and QCD multijet production enter the signal region selection via misidentification of jets as leptons or from selecting leptons that originate from decays of hadrons. The W+jets background is estimated from a data sample where one of the leptons passes only a looser selection than the tight signal region isolation and identification criteria. This sample is enriched in the W+jets process and the contributions from other processes are estimated from MC samples and subtracted. To estimate the contribution in the signal region the sample is reweighted using extrapolation factors ("fake factors"). The factors are derived from the ratio of the number of jets that pass the tight lepton selection to the number of jets that pass the loose lepton selection in a dijet enriched data sample. The QCD contribution is estimated in a similar way, using a data sample with 2 leptons that

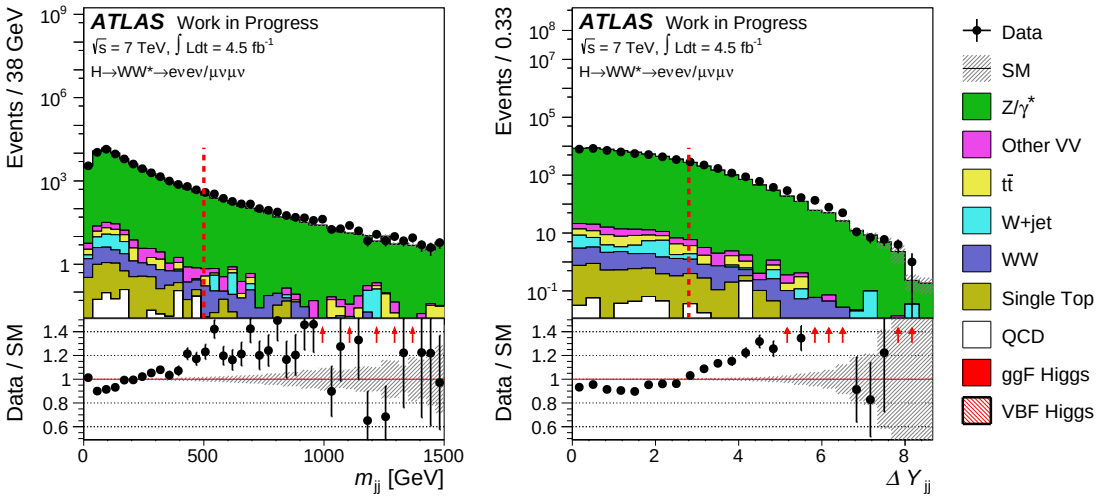

Figure 4.13: The m_{jj} (left) and ΔY_{jj} (right) distribution in the Z-peak control region. The dashed red line indicates the lower bound where the cut is applied. The mismodelling shown here has only a small impact on the results since it affects the normalisation of the $Z/\gamma^* \to \tau\tau$ background that contributes only only 9% in the $e\mu/\mu e$ and 12% in the $ee/\mu\mu$ channel with a MC stat. uncertainty of 71% and 50%. For $Z/\gamma^* \to ee/\mu\mu$ the mismodelling seen in Alpgen MC is covered by the 39% uncertainty of the ABCD method.

pass only the loosened selection. The contribution of W+jets and QCD is small in the signal region of this analysis since it is effectively suppressed by the $p_{\mathrm{T}}^{\mathrm{tot}}$ cut and the dijet requirements (see Wj/jj in tables 4.9 and 4.10).

4.4 Cutflows and Plots

The MC prediction and the number of observed data events after each step of the signal region selection ("Cutflow") provides a check for the impact of the cuts and the agreement between data and MC prediction. Before unblinding, cutflows and distributions of the key variables in the first stages of the signal region selection have been checked using a selection where the blinding criteria are applied for both data and MC. The unblinded cutflows can be seen in tables 4.7 and 4.8. Detailed tables with the single background processes listed separately and the normalisation factors at each step can be found in Appendix A. The top NFs from table 4.4 and the cut efficiency corrections for Z+jets from table 4.6 are applied at the corresponding steps in the cutflow. The total $Z/\gamma^* \to ee/\mu\mu$ NF from table 4.5 is applied starting from the $m_{\ell\ell}$ cut stage since the ABCD method makes a prediction for the region with the $m_{\ell\ell}$ cut applied. The $Z \to \tau\tau$ NF is applied from the $Z \to \tau\tau$ veto downwards. The distributions of the observables that are cut on are

shown in figures 4.14 - 4.21. Each observable is plotted at the stage in the cutflow right before it is cut on. The $m_{\ell\ell}$, $\Delta\phi_{\ell\ell}$ and m_{T} distribution are additionally shown after the $Z \to \tau\tau$ veto since statistics are very low after the dijet (m_{jj} and ΔY_{jj}) cuts which makes the comparison of the shapes difficult. Within the uncertainties, agreement of data and MC predictions can be seen both in the plots and cutflows.

$e\mu/\mu e$	VBF+VH	Total Bkg.(+ggF)	Observed	Data/MC
Preselection	13.05 ± 0.13	20732 ± 59	21109	1.02 ± 0.01
at least two jets	6.65 ± 0.09	7861 ± 21	8042	1.02 ± 0.01
b-jet veto	4.69 ± 0.07	925 ± 9	949	1.03 ± 0.03
$p_{\mathrm{T}}^{\mathrm{tot}} < 15$ GeV	3.76 ± 0.06	584 ± 7	619	1.06 ± 0.04
$Z \to \tau\tau$ veto	3.18 ± 0.05	306 ± 5	310	1.01 ± 0.06
$m_{\mathrm{jj}} > 500$ GeV	1.14 ± 0.02	13.31 ± 0.73	13	0.98 ± 0.28
$\Delta Y_{\mathrm{jj}} > 2.8$	1.12 ± 0.02	10.05 ± 0.55	11	1.09 ± 0.34
CJV (20 GeV)	1.04 ± 0.02	7.23 ± 0.49	8	1.11 ± 0.40
Outside lepton veto	1.00 ± 0.02	5.93 ± 0.46	6	1.01 ± 0.42
$\Delta\phi_{\ell\ell} < 1.8$	0.90 ± 0.02	3.60 ± 0.36	4	1.11 ± 0.57
$m_{\ell\ell} < 50$ GeV	0.77 ± 0.02	1.62 ± 0.24	2	1.23 ± 0.89
$m_{\mathrm{T}} < 130$ GeV	0.71 ± 0.01	0.80 ± 0.15	0	0

Table 4.7: Cutflow for the $e\mu/\mu e$ channel. The errors are the statistical uncertainties. The background prediction is normalised as described in section 4.4

$ee/\mu\mu$	VBF+VH	Total Bkg.(+ggF)	Observed	Data/MC
$\not{E}_T > 45$ GeV	7.67 ± 0.10	11086 ± 55	11676	1.05 ± 0.01
at least two jets	4.24 ± 0.07	5022 ± 18	5056	1.01 ± 0.01
b-jet veto	2.95 ± 0.05	824 ± 10	860	1.04 ± 0.04
$p_{\mathrm{T}}^{\mathrm{tot}} < 15$ GeV	2.36 ± 0.05	522 ± 8	535	1.02 ± 0.05
$Z \to \tau\tau$ veto	1.94 ± 0.04	315 ± 6	327	1.04 ± 0.06
$m_{\mathrm{jj}} > 500$ GeV	0.74 ± 0.02	21.00 ± 1.45	15	0.71 ± 0.19
$\Delta Y_{\mathrm{jj}} > 2.8$	0.72 ± 0.02	14.26 ± 1.17	11	0.77 ± 0.24
CJV (20 GeV)	0.67 ± 0.01	9.23 ± 1.06	5	0.54 ± 0.25
Outside lepton veto	0.64 ± 0.01	6.63 ± 0.70	5	0.75 ± 0.35
$\Delta\phi_{\ell\ell} < 1.8$	0.57 ± 0.01	3.89 ± 0.54	4	1.03 ± 0.53
$m_{\ell\ell} < 50$ GeV	0.51 ± 0.01	1.84 ± 0.37	4	2.17 ± 1.17
$m_{\mathrm{T}} < 130$ GeV	0.47 ± 0.01	1.27 ± 0.31	4	3.14 ± 1.75

Table 4.8: Cutflow for the $ee/\mu\mu$ channel. The errors are the statistical uncertainties. The background prediction is normalised as described in section 4.4

$e\mu/\mu e$	ggF	Diboson	Top	$Z \to \ell\ell$	$Z \to \tau\tau$	Wj/jj
Preselection	80.21	2205.44	8748.47	229.68	8511.82	952.24
at least two jets	10.64	197.21	7048.53	18.87	485.60	98.04
b-jet veto	7.57	141.03	383.44	13.52	329.28	48.99
$p_{\mathrm{T}}^{\mathrm{tot}} < 15$ GeV	4.83	100.13	217.04	7.68	243.35	9.32
$Z \to \tau\tau$ veto	4.16	60.74	141.38	4.37	88.65	6.07
$m_{\mathrm{jj}} > 500$ GeV	0.36	3.37	7.18	0.06	2.32	< 0.07
$\Delta Y_{\mathrm{jj}} > 2.8$	0.35	2.91	5.37	0.06	1.31	< 0.09
CJV (20 GeV)	0.25	2.50	3.47	negl.	0.94	< 0.11
Outside lepton veto	0.23	1.87	3.19	negl.	0.56	< 0.12
$\Delta\phi_{\ell\ell} < 1.8$	0.20	1.16	1.85	negl.	0.29	< 0.12
$m_{\ell\ell} < 50$ GeV	0.18	0.45	0.73	negl.	0.21	< 0.08
$m_{\mathrm{T}} < 130$ GeV	0.16	0.20	0.35	negl.	0.07	< 0.02

Table 4.9: Background composition for the $e\mu/\mu e$ channel. The background prediction is normalised as described in section 4.4. The upper bounds on the Wj/jj backgrounds are the 1σ stat. errors added to the estimated values. Negative values that originate from the background subtraction procedure were set to 0.

$ee/\mu\mu$	ggF	Diboson	Top	$Z \to \ell\ell$	$Z \to \tau\tau$	Wj/jj
Preselection	39.73	879.92	5066.28	4274.80	664.16	152.76
at least two jets	6.23	106.95	4111.18	590.24	178.94	23.79
b-jet veto	4.33	75.10	231.83	390.09	116.62	3.56
$p_{\mathrm{T}}^{\mathrm{tot}}$ <15 GeV	2.68	52.16	128.49	252.64	84.05	0.30
$Z \to \tau\tau$ veto	2.25	34.35	90.13	164.22	22.75	0.38
$m_{\mathrm{jj}} > 500$ GeV	0.16	2.33	5.13	11.76	1.35	< 0.35
$\Delta Y_{\mathrm{jj}} > 2.8$	0.15	1.97	3.85	7.29	0.80	< 0.26
CJV (20 GeV)	0.11	1.64	2.62	4.11	0.59	< 0.22
Outside lepton veto	0.10	1.33	2.41	2.34	0.27	< 0.24
$\Delta\phi_{\ell\ell} < 1.8$	0.10	0.91	1.08	1.50	0.24	< 0.06
$m_{\ell\ell} < 50$ GeV	0.09	0.30	0.37	0.88	0.18	< 0.01
$m_{\mathrm{T}} < 130$ GeV	0.08	0.12	0.16	0.71	0.16	< 0.01

Table 4.10: Background composition for the $ee/\mu\mu$ channel. The background prediction is normalised as described in section 4.4. The upper bounds on the Wj/jj backgrounds are the 1σ stat. errors added to the estimated values. Negative values that originate from the background subtraction procedure were set to 0.

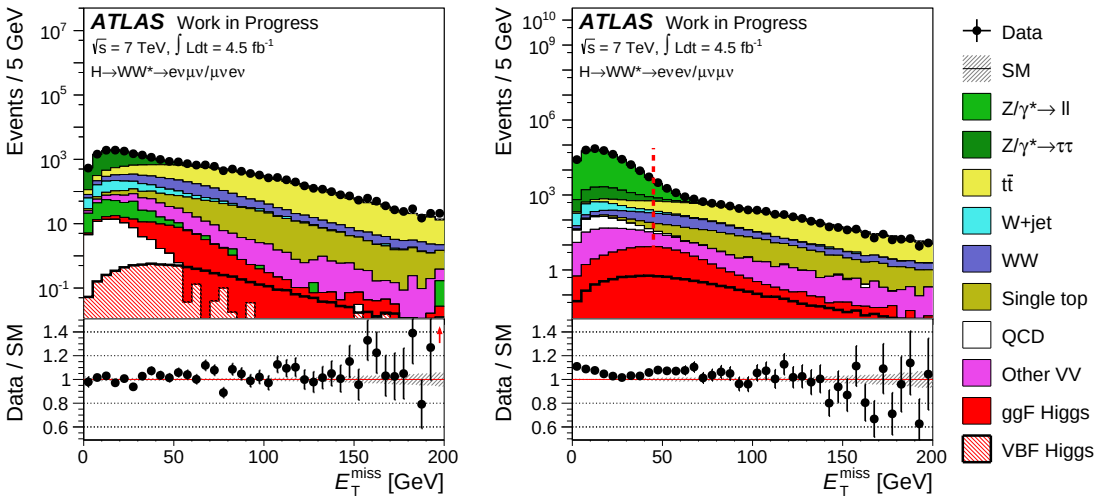

Figure 4.14: The $\not\!\!E_T$ distribution after the preselection and the Z veto. For $e\mu/\mu e$ (left) no cut on $\not\!\!E_T$ is applied. For $ee/\mu\mu$ (right) the lower bound on $\not\!\!E_T$ reduces the low peaking $Z/\gamma^* \rightarrow ee/\mu\mu$ background

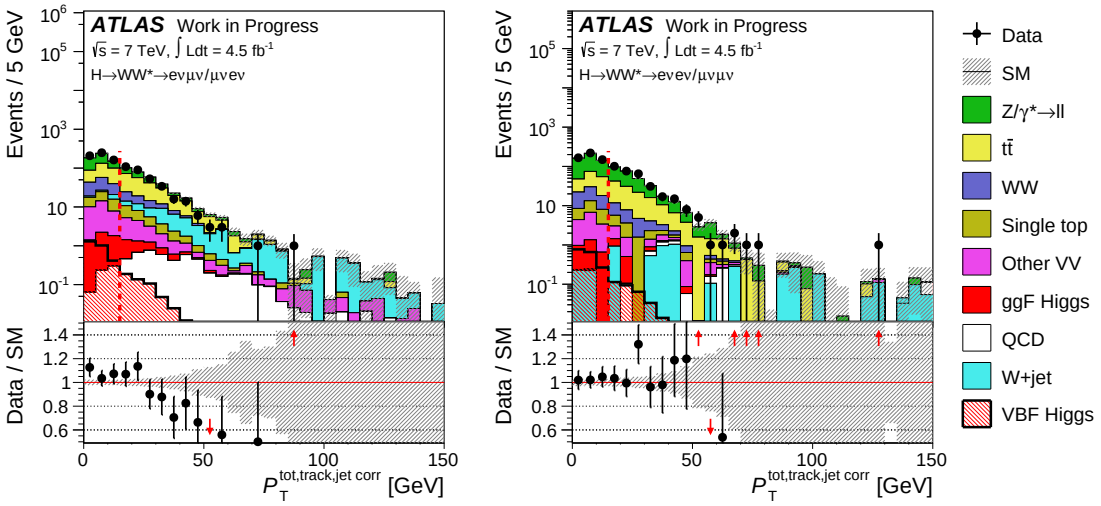

Figure 4.15: The $p_{\mathrm{T}}^{\mathrm{tot}}$ distribution after the b veto for $e\mu/\mu e$ (left) and $ee/\mu\mu$ (right). The upper bound leads to cleaner events and suppresses the fake backgrounds W+jets and QCD

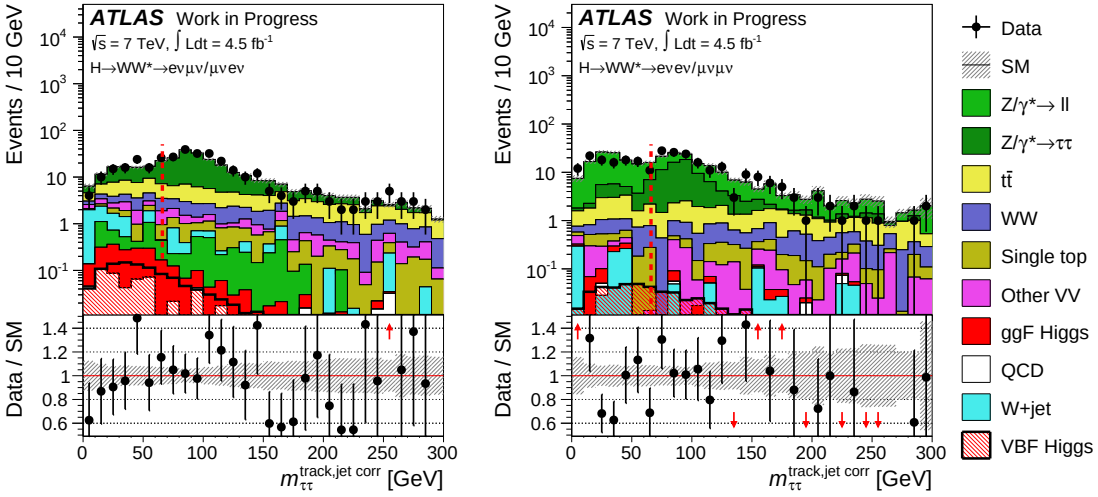

Figure 4.16: The $m_{\tau\tau}$ distribution after the $p_{\mathrm{T}}^{\mathrm{tot}}$ cut for $e\mu/\mu e$ (left) and $ee/\mu\mu$ (right). The upper bound reduces the $Z/\gamma^* \to \tau\tau$ contribution ("$Z \to \tau\tau$ veto")

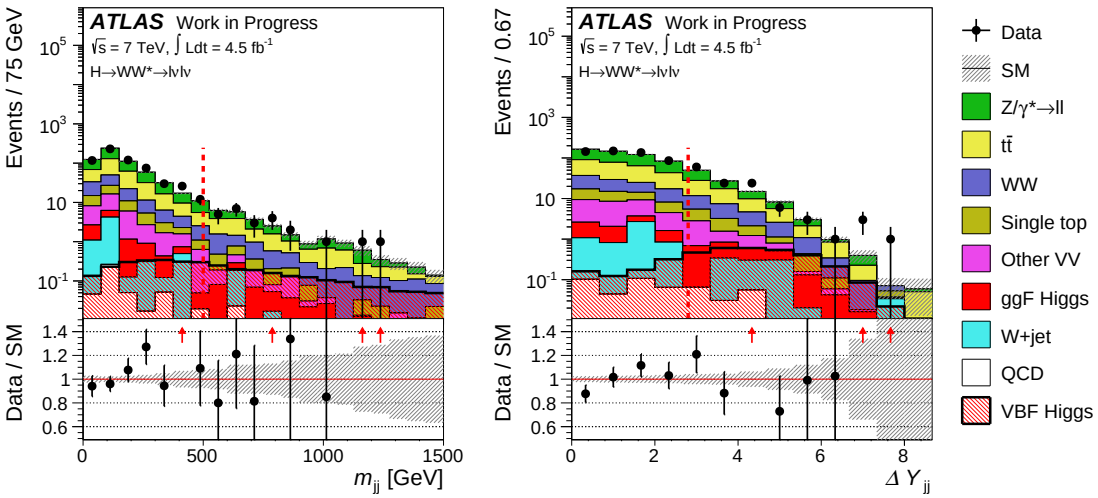

Figure 4.17: The m_{jj} (left) and ΔY_{jj} (right) distribution after the $Z \to \tau\tau$ veto. All lepton flavour channels are combined. The lower bound requirements on these dijet variables significantly enhance the VBF signal fraction

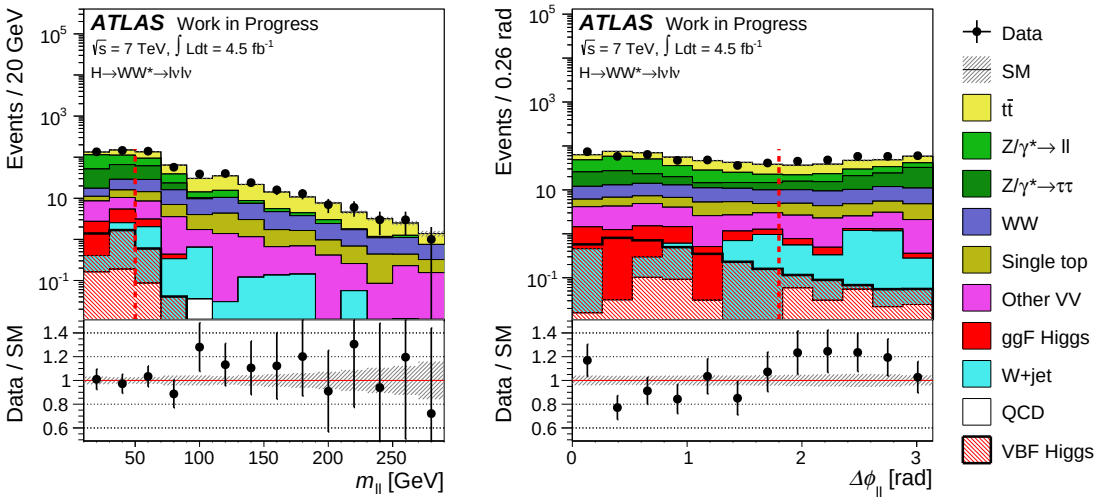

Figure 4.18: The $m_{\ell\ell}$ (left) and $\Delta\phi_{\ell\ell}$ (right) distribution after the $Z \to \tau\tau$ veto. All lepton flavour channels are combined. Upper bounds on these dilepton properties are the most distinctive features of the $H \to WW \to \ell\nu\ell\nu$ decay

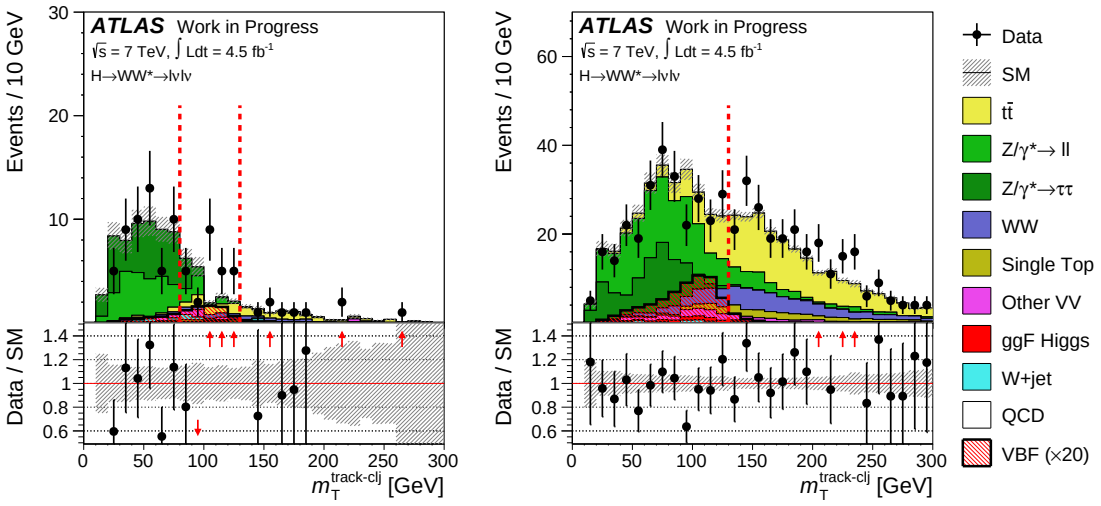

Figure 4.19: The m_{T} distribution for $p_{\mathrm{T}}^{\mathrm{sublead}} < 15\,\mathrm{GeV}$ (left) and $p_{\mathrm{T}}^{\mathrm{sublead}} > 15\,\mathrm{GeV}$ (right) after the $Z \to \tau\tau$ veto. The remaining Z background has a peak at lower values for the low $p_{\mathrm{T}}^{\mathrm{sublead}}$ events which motivates an additional lower bound on m_{T} in this case. The signal is scaled by a factor of 20 to make the distribution visible in the linear scale plot. All lepton flavor channels are combined.

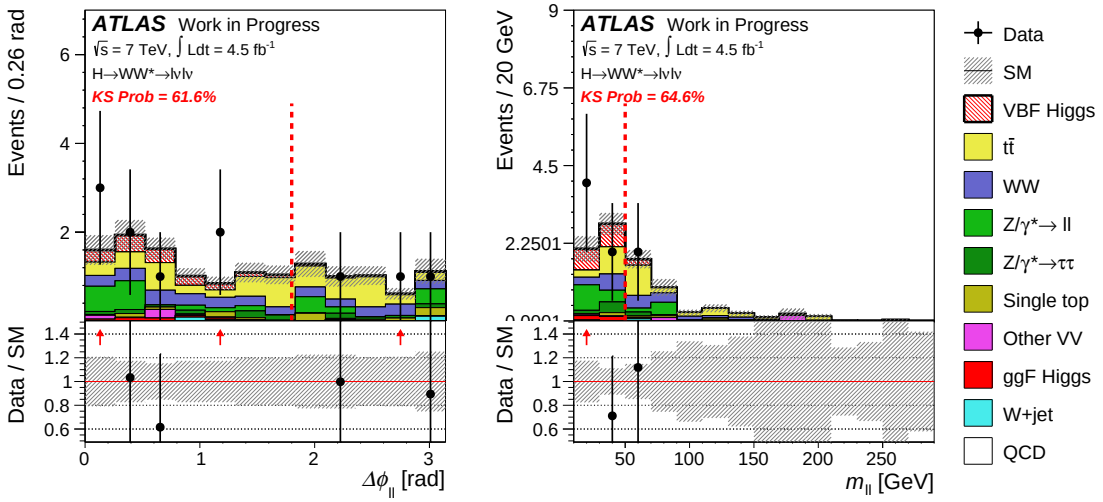

Figure 4.20: The $\Delta\phi_{\ell\ell}$ distribution after the OLV cut (left) and $m_{\ell\ell}$ distribution after $\Delta\phi_{\ell\ell}$ cut (right). All lepton flavour channels are combined.

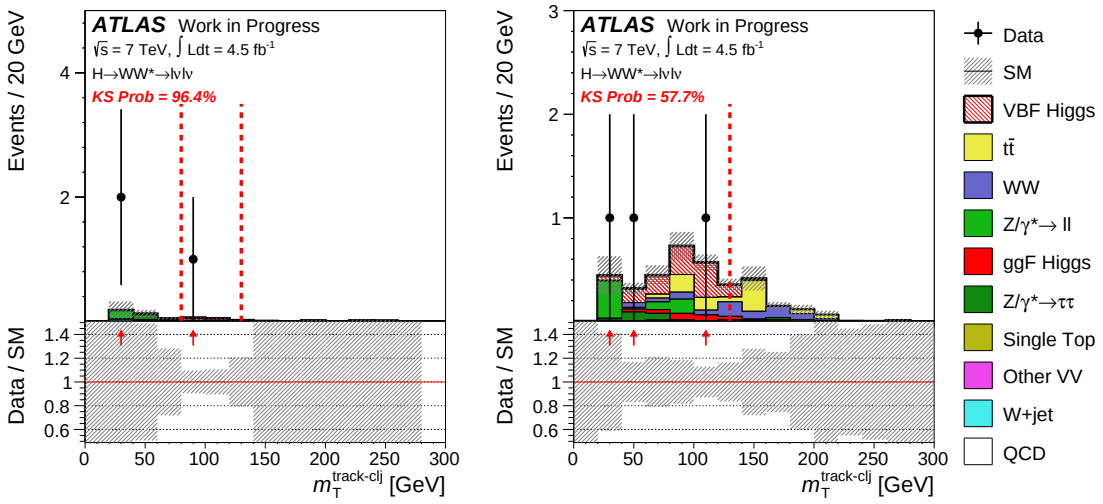

Figure 4.21: The m_{T} distribution with all the other cuts applied for $p_{\mathrm{T}}^{\mathrm{sublead}} < 15\,\mathrm{GeV}$ (left) and $p_{\mathrm{T}}^{\mathrm{sublead}} > 15\,\mathrm{GeV}$ (right). All lepton flavor channels are combined

4.5 Uncertainties

4.5.1 Statistical uncertainty

The analysis is mainly limited by the low number of expected events and hence the statistical uncertainties. The extraction of quantities from the number of N observed data events has the standard deviation (s.d.) $\sqrt{N}$ as a statistical uncertainty. This affects the uncertainty on the measured signal strength (see section 4.6) and the uncertainty on background normalisation from control regions which are sparsely populated by data events (e.g the top NF). The errors on the NFs given in the tables of the previous sections are calculated using the sum in quadrature (Gaussian error propagation) of the MC stat. error from Eq. (4.1) and the data s.d. $\sqrt{N}$. The significance of a potential signal is also constrained by the low number of expected events since fluctuations of observed data can cover the expected signal, even in case of a background only hypothesis (more in section 4.6).

4.5.2 Experimental uncertainties

Systematic uncertainties can be induced by experimental uncertainties. These include resolution, efficiency and energy scale uncertainties for the objects in the analysis. The 1σ variations are determined in the ntuple production stage. A new set of ntuples is produced for each variation that affects the object selection. For the other uncertainties event weights are stored that account for the 1σ up and down variation caused by the respective uncertainty. For the uncertainties for the lepton and jet selection the analysis follows the recommendations of the ATLAS performance groups. In the VBF analysis the largest contribution is coming from the jet uncertainties, namely the energy scale (JES), the jet energy resolution (JER) and b tagging uncertainties. Table 4.11 shows a summary for the experimental uncertainties as they were determined from 7 TeV MC. Due to low MC statistics in the signal region of the 7 TeV analysis the large uncertainties on the background are driven by statistical fluctuations. Therefore, for the fit (section 4.6) only the largest uncertainty coming from the JES η modelling as it was determined from 8 TeV MC is used (see table 4.15).

4.5.3 Theoretical uncertainties

A large contribution to the systematic uncertainty on the prediction of expected background and signal comes from "theoretical" uncertainties. Those include the uncertainty on the cross section (total cross section and matrix element), PDFs, parton shower and QCD scale. The prediction of backgrounds that are normalised using data is independent

	Signal $e\mu/\mu e$	Background $e\mu/\mu e$	Signal $ee/\mu\mu$	Background $ee/\mu\mu$
SR				
Jets	$^{+7.4\%}_{-7.6\%}$	$^{+27.0\%}_{-39.8\%}$	$^{+8.5\%}_{-7.8\%}$	$^{+47.0\%}_{-56.5\%}$
Leptons	$^{+2.8\%}_{-2.7\%}$	$^{+7.9\%}_{-18.0\%}$	$^{+2.5\%}_{-2.4\%}$	$^{+14.4\%}_{-16.9\%}$
$\not{E}_T$	$^{+1.2\%}_{-1.3\%}$	$^{+6.4\%}_{-12.7\%}$	$^{+1.2\%}_{-1.5\%}$	$^{+19.6\%}_{-26.1\%}$
Top CR				
jets		$^{+13.4\%}_{-14.6\%}$		$^{+12.1\%}_{-8.1\%}$
leptons		$^{+3.0\%}_{-3.2\%}$		$^{+7.5\%}_{-2.1\%}$
$\not{E}_T$		$^{+2.8\%}_{-5.4\%}$		$^{+4.1\%}_{-5.4\%}$

Table 4.11: Summary for the experimental uncertainties. The values for the up and down variations correspond to the sum in quadrature of all contributing 1σ impacts on the predicted signal or background yield. The uncertainties where determined with 7 TeV MC. Since the large uncertainties on the background in the signal region are driven by statistical fluctuations from the low MC statistics uncertainties determined from 8 TeV MC are used in the final fit.

of total cross section uncertainties. The uncertainty is given by the extrapolation from the control region to the signal region. The expected number of background events in the signal region can be seen as extrapolating the number of data events in the control region to the signal region by an extrapolation factor α which is the ratio of the number of MC events in the signal region to the number of MC events in the control region:

$$N_{\text{SR}} = \underbrace{\frac{N_{\text{CR, data}}}{N_{\text{CR, MC}}}}_{NF} N_{\text{SR, MC}} = \underbrace{\frac{N_{\text{SR, MC}}}{N_{\text{CR, MC}}}}_{\alpha} N_{\text{CR, data}}$$

The uncertainty on α is determined by varying theoretical parameters like the QCD scale or the PDF uncertainties and by comparing different MC generators and showering programs. Since the different MC samples were only available for the 8 TeV run these uncertainties are taken from the 8 TeV analysis. The uncertainties are expected to increase with tighter constraints on the observables so in the context of the loosened cuts in the 7 TeV analysis the theory uncertainties determined with 8 TeV MC and cuts should be a conservative estimate. Table 4.12 shows the theory uncertainties on the major backgrounds and the signal. The uncertainty of the $Z/\gamma^* \to ee/\mu\mu$ background estimation is given by the ABCD systematic uncertainty of 39% (see section 4.3.2) which was determined with 7 TeV MC.

Process	Uncertainty	Source
VBF signal	10%	QCD scale, generator modelling, PS/UE, CJV, PDF
ggF Higgs	56%	QCD scale, PDF, generator modelling, PS/UE
WW	35%	QCD scale, generator modelling
Top	26%	QCD scale, generator modelling, PS, PDF (on α)

Table 4.12: Total (sum in quadrature) theory uncertainties the VBF signal, the ggF Higgs production, the WW and the top background. The uncertainties where determined with 8 TeV MC. PS stands for parton shower, UE for underlying event and CJV for the uncertainty due to introducing the central jet veto.

4.6 Statistics

The statistical procedure uses a frequentist approach similar to the one reported in [42]. In frequentist statistics the expectation (model) is interpreted to predict the frequency of a certain outcome when an experiment is often repeated. The first step of discovering a new signal is usually done by rejecting a "null hypothesis" with no signal. This is done by constructing a test statistic t_μ which can for example be a probability density function (p.d.f) of a signal strength parameter μ. In this case the "local p_0 value" is given by the probability of measuring the observed or a higher value of μ under the assumption of the test statistic at $\mu = 0$. The probability can be converted to a hypothetical number of standard deviations ("significance") of a Gaussian distribution

$$Z_0 = \Phi^{-1}(1 - p_0)$$

where Φ is the inverse cumulative distribution function of a Gaussian. In particle physics the usual convention is to claim an "observation" when $Z_0 > 5$.
The probability p to measure a given set of data as a function of the regarded model is called "likelihood" L.

$$p(\text{data}|\text{model}) = L(\text{model})$$

A model is written in terms of several parameters ("estimators") $\boldsymbol{\theta} = (\theta_1, \ldots, \theta_n)$. The model that fits best to the data can be determined by maximising the Likelihood ("fit"). The parameters that maximise the likelihood (ML estimators) are denoted by $\hat{\boldsymbol{\theta}}$.
The results presented in section 4.7 where determined by using a likelihood function that consists of Poisson p.d.fs for each signal and control region.

$$f_{\text{Poisson}}(N|\lambda) = \frac{e^{-\lambda}\lambda^N}{N!}$$

The total number of expected events in each region is parametrised as

$$\lambda = \mu s + b$$

with the signal strength μ and the number of expected signal events s and the sum of all expected background events b. Each process that is normalised in a CR is multiplied by the NF both in the SR and CR. The NFs are estimators in the likelihood. To incorporate systematic uncertainties they are also treated as estimators in the likelihood ("nuisance parameters"). The parameters θ_{sys} are constrained by unit Gaussian p.d.fs. To describe their impact on the normalisation of certain processes the expected yields in the λ parameter of the Poisson p.d.fs for the signal and control regions are multiplied by response functions $\nu(\theta_{sys})$. They are constructed such that $\theta_{sys} = \pm 1$ corresponds to the $\pm 1\sigma$ uncertainty. Systematic uncertainties use an exponential response function which is in combination with the Gaussian constraint equivalent to using linear response functions and a log normal constraint. MC stat. uncertainties are described by estimators that are constrained by Poisson p.d.fs and linear response functions.
Hypothesis testing is done using the "profile likelihood ratio" test statistic

$$q_\mu = -2 \ln \frac{L(\mu, \hat{\hat{\boldsymbol{\theta}}})}{L_{\max}}$$

where the $\hat{\hat{\boldsymbol{\theta}}}$ are the values that maximise the likelihood for the given value μ and $L_{\max}$ is the maximum likelihood in all parameters (including μ). In case that the ML estimator $\hat{\mu}$ is negative $L_{\max}$ is determined for $\mu = 0$ (background only). One concrete property of q_μ is that the significance for rejecting the null hypothesis ($\mu = 0$) can be approximated as [43]

$$Z_0 = \sqrt{q_0}$$

The "expected" significance is given by maximising the likelihood for the "Asimov dataset" which is generated by inserting the expected mean values for s and b and $\mu = 1$. The total uncertainty on the signal strength is determined by solving the equation $q_\mu = 1$ for the 1σ variation.

4.7 Results

The fit has been performed using the parameters from table 4.15. Table 4.16 shows the fit values for the normalisation factors. The expected significance for all channels combined is 0.82σ, the observed significance is 0.08σ. The measured signal strength is $0.16^{+1.8}_{-1.2}$. table 4.13 shows the results for the $ee/\mu\mu$ and $e\mu/\mu e$ subchannels and the split into statistical and systematic uncertainties for the signal strength. Since there are no data events in the $e\mu/\mu e$ category (see table 4.7) no signal strength and only the expected significance value is given there. The fit has also been performed in combination with the 8 TeV cut based analysis (see table 4.14). The combination was done in an overall fit for the 0, 1 and ≥ 2 jet channels with two separate signal strength parameters for ggF production (μ_{ggF})

and VBF production (μ_{VBF}). The result for μ_{VBF} is an expected significance of 2.1σ and an observed significance of 3.0σ. The observed signal strength is $1.5^{+0.8}_{-0.6}$. This gives a consistent cross check for the more sensitive BDT analysis which gives an expected significance of 2.7σ and an observed significance of 3.2σ at a signal strength of $1.3^{+0.5}_{-0.4}$ in a similar combination.

7 TeV cut based	$e\mu/\mu e$	$ee/\mu\mu$	combined
Z_0^{exp}	0.72	0.39	0.82
Z_0^{obs}	-	1.72	0.08
$\hat{\mu}$	-	5.66	0.16
Stat. err.	-	$^{+5.0}_{-3.6}$	$^{+1.9}_{-1.5}$
Sys. err.	-	$^{+2.6}_{-1.3}$	$^{+1.0}_{-1.2}$
Tot. err.	-	$^{+5.6}_{-3.8}$	$^{+2.1}_{-1.9}$

Table 4.13: Expected and observed significance levels and the observed signal strength $\hat{\mu}$ for $e\mu/\mu e$, $ee/\mu\mu$ and the combined fit for of both channels. The given errors are the 1σ impact on the signal strength.

cut based	7 TeV	8 TeV	combined
Z_0^{exp}	0.82	1.95	2.07
Z_0^{obs}	0.08	3.17	2.95
$\hat{\mu}$	0.16	1.72	1.5
Stat. err.	$^{+1.9}_{-1.5}$	$^{+0.71}_{-0.61}$	$^{+0.61}_{-0.53}$
Sys. err.	$^{+1.0}_{-1.2}$	$^{+0.43}_{-0.28}$	$^{+0.39}_{-0.26}$
Tot. err.	$^{+2.1}_{-1.9}$	$^{+0.83}_{-0.67}$	$^{+0.72}_{-0.60}$

Table 4.14: Expected and observed significance levels and the observed signal strength $\hat{\mu}$ for the cut based 7 TeV and 8 TeV analyses and the combination. The given errors are the 1σ impact on the signal strength.

Fit parameters	SR $ee/\mu\mu$	SR $e\mu/\mu e$	Top $e\mu/\mu e$	Top $ee/\mu\mu$	B	C	D
Nuisance parameters							
JES η modelling bkg. (sig.)	7% (7%)	9% (5%)	11%	11%			
VBF theory	9% (VBF)	9% (VBF)					
ggF theory	56% (ggF)	56% (ggF)					
Top theory/extrapolation	26% (top)	26% (top)					
WW theory	35% (WW)	35% (WW)					
ABCD, CF stat.	42% (Z)						
Fitted NFs							
NF_{Top}	✓	✓	✓	✓			
$Ratio_{BD}$	✓				✓		
NF_C	✓					✓	
NF_D					✓		✓
Fixed correction factors							
$Z \to \tau\tau$ CF	1.44 ($Z\tau\tau$)	1.44 ($Z\tau\tau$)					
$Z \to \ell\ell$ CF	1.15 ($Z\ell\ell$)						

Table 4.15: Parameters for the likelihood fit. The nuisance parameters are taken from the 8 TeV analysis except for the Z uncertainty which is combined from the uncertainty on the ABCD method (39%) and the statistical uncertainty on the correction factor (16%). The regions B, C and D are the Z control regions for the ABCD method. The fixed correction factors are not fitted (for their calculation see section 4.3).

Normalisation Factors	calculated	determined from fit
NF_{ABCD}	1.12 ± 0.23	1.09 ± 0.18 $(= \text{Ratio}_{BD} \times \text{NF}_C)$
NF_{Top}	1.30 ± 0.43	1.26 ± 0.41

Table 4.16: The normalisation factor for the top background and the ABCD NF for the $Z \to \ell\ell$ background. The left column shows the values that were calculated as described in section 4.3, the right column shows the values that were determined from the likelihood fit.

Chapter 5

Conclusion and Outlook

A cut based analysis of the VBF $H \to WW$ process with ATLAS $\sqrt{s}$ =7 TeV data from 2011 has been presented. The goal was a combination with a similar analysis on the larger $\sqrt{s}$ =8 TeV dataset from 2012 to support and cross check a multivariate boosted decision tree analysis that was done in parallel. To simplify the combination the analysis was designed similar to the $\sqrt{s}$ =8 TeV analysis. Modifications that were made to account for the lower statistics in the 2011 dataset consist of less restrictive selection requirements and the statistical evaluation by a cut and count approach instead of a fit on the transverse mass distribution. The combined result from the $\sqrt{s}$ =7 TeV and the $\sqrt{s}$ =8 TeV analyses gives a consistent cross check to the BDT analysis which gives evidence for the VBF production mode in the $H \to WW$ decay channel.
More data and the higher centre of mass energy of $\sqrt{s}$ =13 TeV in the next LHC run will establish an observation for this channel if the observed particle has the properties of a standard model Higgs boson. The increased statistics will allow the precise determination of the Higgs boson couplings to the electroweak gauge bosons using the VBF $H \to WW$ channel. This can be compared to the fermionic couplings from other processes to further test the standard model predictions or find deviations that can hint to new physics.

Appendix A

Cutflows

	VBF+VH [125 GeV]	ggF [125 GeV]	WW	other diboson	Top	$Z \to ee/\mu\mu$+jets	$Z \to \tau\tau$+jets	W+jets + QCD	Total Bkg.(+ggF)	Observed	Data/MC
Object selection	15.82 ± 0.15	89.96 ± 0.37	1983.24 ± 4.74	1400.04 ± 6.92	9056.85 ± 19.21	2860544.02 ± 1500.10	9807.66 ± 56.27	8610.92 ± 52.02	2892974.32 ± 1502.21	2920141	1.01 ± 0.00
lepton p_T	15.57 ± 0.15	87.91 ± 0.36	1970.28 ± 4.73	1373.30 ± 6.83	9017.03 ± 19.16	2756967.39 ± 1482.30	8915.58 ± 53.86	8113.67 ± 51.82	2787914.80 ± 1484.34	2871248	1.03 ± 0.00
OS leptons	14.46 ± 0.13	87.77 ± 0.36	1964.26 ± 4.72	1067.44 ± 5.34	8969.61 ± 19.11	2750728.52 ± 1481.17	8892.01 ± 53.79	7489.78 ± 50.75	2780665.33 ± 1483.16	2865410	1.03 ± 0.00
$m_{\ell\ell} > 12, 10$ GeV	14.20 ± 0.13	85.39 ± 0.36	1956.25 ± 4.71	1042.36 ± 5.17	8942.65 ± 19.08	2745947.00 ± 1480.80	8828.60 ± 53.69	7163.30 ± 49.19	2775418.56 ± 1482.73	2847522	1.03 ± 0.00
Z veto (for ee,$\mu\mu$)	13.42 ± 0.13	84.26 ± 0.36	1533.63 ± 4.17	402.02 ± 4.10	7052.74 ± 16.95	294372.45 ± 456.58	8497.01 ± 52.65	2201.74 ± 26.91	314410.01 ± 460.74	333075	1.06 ± 0.00
$E_T^{miss} > 45$ GeV (SF)	7.67 ± 0.10	39.73 ± 0.24	773.59 ± 2.94	106.33 ± 2.13	5066.28 ± 14.37	4274.80 ± 50.56	664.16 ± 12.45	152.76 ± 6.76	11086.19 ± 54.56	11676	1.05 ± 0.01
Scale factors					NF = 1.03						
at least two jets	4.24 ± 0.07	6.23 ± 0.10	81.91 ± 0.93	25.04 ± 1.06	4111.18 ± 13.30	590.24 ± 10.64	178.94 ± 5.13	23.79 ± 4.24	5022.40 ± 18.34	5056	1.01 ± 0.01
Scale factors					NF = 1.03	NF = 0.96	NF = 0.95				
b-jet veto	2.95 ± 0.05	4.33 ± 0.08	57.88 ± 0.78	17.22 ± 0.89	231.83 ± 3.08	390.09 ± 8.62	116.62 ± 4.04	3.56 ± 2.24	824.45 ± 10.32	860	1.04 ± 0.04
Scale factors					NF = 1.09	NF = 0.95	NF = 0.93				
$p_{T,tot} < 15$ GeV	2.36 ± 0.05	2.68 ± 0.06	40.60 ± 0.65	11.56 ± 0.77	128.49 ± 2.34	252.64 ± 7.12	84.05 ± 3.53	0.30 ± 0.71	522.27 ± 8.38	535	1.02 ± 0.05
Scale factors					NF = 1.09	NF = 0.95	NF = 0.97				
$Z \to \tau\tau$ veto	1.94 ± 0.04	2.25 ± 0.06	26.28 ± 0.52	8.07 ± 0.64	90.13 ± 1.95	164.22 ± 5.60	22.75 ± 1.85	0.38 ± 0.57	314.88 ± 6.29	327	1.04 ± 0.06
Scale factors					NF = 1.18	NF = 1.32	NF = 1.40				
$m_{jj} > 500$ GeV	0.74 ± 0.02	0.16 ± 0.02	1.84 ± 0.11	0.49 ± 0.19	5.13 ± 0.50	11.76 ± 1.30	1.35 ± 0.29	0.17 ± 0.18	21.00 ± 1.45	15	0.71 ± 0.19
Scale factors					NF = 0.99	NF = 1.37	NF = 1.48				
$\Delta Y_{jj} > 2.8$	0.72 ± 0.02	0.15 ± 0.02	1.60 ± 0.10	0.37 ± 0.18	3.85 ± 0.39	7.29 ± 1.05	0.80 ± 0.21	0.13 ± 0.13	14.26 ± 1.17	11	0.77 ± 0.24
Scale factors					NF = 1.21	NF = 1.56	NF = 1.55				
central jet veto (20 GeV)	0.67 ± 0.01	0.11 ± 0.01	1.36 ± 0.09	0.28 ± 0.17	2.62 ± 0.35	4.11 ± 0.96	0.59 ± 0.20	0.10 ± 0.12	9.23 ± 1.06	5	0.54 ± 0.25
Scale factors					NF = 1.33	NF = 1.52	NF = 1.50				
Outside lepton veto	0.64 ± 0.01	0.10 ± 0.01	1.13 ± 0.08	0.20 ± 0.16	2.41 ± 0.36	2.34 ± 0.56	0.27 ± 0.10	0.12 ± 0.12	6.63 ± 0.70	5	0.75 ± 0.35
Scale factors					NF = 1.33	NF = 1.52	NF = 1.50				
$\Delta\phi_{\ell\ell} < 1.8$	0.57 ± 0.01	0.10 ± 0.01	0.72 ± 0.07	0.19 ± 0.16	1.08 ± 0.23	1.50 ± 0.45	0.24 ± 0.09	0.02 ± 0.04	3.89 ± 0.54	4	1.03 ± 0.53
Scale factors					NF = 1.33	NF = 1.29	NF = 1.50				
$m_{\ell\ell} < 50$ GeV	0.51 ± 0.01	0.09 ± 0.01	0.28 ± 0.04	0.02 ± 0.00	0.37 ± 0.13	0.88 ± 0.33	0.18 ± 0.08	−0.02 ± 0.01	1.84 ± 0.37	4	2.17 ± 1.17
Scale factors					NF = 1.33	NF = 1.29	NF = 1.50				
$m_T < 130$ GeV	0.47 ± 0.01	0.08 ± 0.01	0.11 ± 0.03	0.01 ± 0.00	0.16 ± 0.09	0.71 ± 0.28	0.16 ± 0.08	−0.01 ± 0.01	1.27 ± 0.31	4	3.14 ± 1.75
Top control region ($n_{b\,jets} = 1$)	1.09 ± 0.04	1.60 ± 0.05	20.59 ± 0.48	6.62 ± 0.54	1362.95 ± 7.44	156.36 ± 5.32	49.17 ± 2.72	13.14 ± 2.79	1612.15 ± 9.97	1672	1.04 ± 0.03
$p_{T,tot} < 15$ GeV	0.77 ± 0.03	0.90 ± 0.04	12.92 ± 0.38	3.76 ± 0.38	759.78 ± 5.54	86.84 ± 4.10	31.16 ± 2.23	0.50 ± 0.90	897.06 ± 7.32	964	1.07 ± 0.04
$Z \to \tau\tau$ veto	0.65 ± 0.03	0.76 ± 0.03	7.86 ± 0.29	2.61 ± 0.33	533.32 ± 4.64	58.89 ± 3.46	7.06 ± 1.05	1.07 ± 0.67	612.12 ± 5.94	655	1.07 ± 0.04
$m_{jj} > 500$ GeV	0.13 ± 0.01	0.05 ± 0.01	0.48 ± 0.05	0.09 ± 0.04	20.38 ± 0.91	3.85 ± 0.64	0.43 ± 0.15	−0.02 ± 0.09	25.39 ± 1.13	29	1.14 ± 0.22
$\Delta Y_{jj} > 2.8$	0.12 ± 0.01	0.05 ± 0.01	0.35 ± 0.05	0.03 ± 0.01	15.45 ± 0.80	1.35 ± 0.37	0.14 ± 0.05	0.00 ± 0.09	17.43 ± 0.88	15	0.86 ± 0.23
central jet veto (20 GeV)	0.11 ± 0.01	0.03 ± 0.01	0.30 ± 0.04	0.01 ± 0.00	5.81 ± 0.48	0.56 ± 0.24	0.06 ± 0.04	0.04 ± 0.08	6.88 ± 0.55	7	1.02 ± 0.39
Outside lepton veto	0.10 ± 0.01	0.03 ± 0.01	0.21 ± 0.03	0.01 ± 0.00	2.95 ± 0.34	0.24 ± 0.15	0.06 ± 0.04	−0.02 ± 0.01	3.53 ± 0.37	5	1.42 ± 0.65
$Z \to \tau\tau$ control region	0.16 ± 0.01	0.17 ± 0.02	1.02 ± 0.11	0.47 ± 0.16	2.50 ± 0.32	23.00 ± 2.03	48.76 ± 2.82	−0.39 ± 0.27	76.01 ± 3.50	72	0.95 ± 0.12
Z control region (lowMET, lowMll)	2.01 ± 0.05	3.59 ± 0.07	5.69 ± 0.25	10.16 ± 0.68	321.30 ± 3.66	10370.94 ± 48.46	145.23 ± 4.99	46.89 ± 5.13	10941.45 ± 49.14	10373	0.95 ± 0.01
b-jet veto	1.41 ± 0.04	2.61 ± 0.06	4.28 ± 0.21	7.51 ± 0.58	15.25 ± 0.76	7301.82 ± 40.26	105.21 ± 4.22	24.12 ± 4.20	7486.72 ± 40.72	6833	0.91 ± 0.01
$p_{T,tot} < 15$ GeV	1.12 ± 0.03	1.65 ± 0.05	3.20 ± 0.19	5.27 ± 0.51	8.86 ± 0.58	5449.83 ± 35.15	81.93 ± 3.84	3.35 ± 1.92	5575.75 ± 35.42	5015	0.90 ± 0.01
$m_{jj} > 500$ GeV	0.37 ± 0.01	0.09 ± 0.01	0.17 ± 0.04	0.06 ± 0.02	0.39 ± 0.12	116.35 ± 3.82	0.55 ± 0.25	−0.77 ± 0.21	119.66 ± 3.85	148	1.24 ± 0.11
$\Delta Y_{jj} > 2.8$	0.37 ± 0.01	0.09 ± 0.01	0.16 ± 0.04	0.06 ± 0.02	0.35 ± 0.11	95.59 ± 3.45	0.31 ± 0.10	−0.55 ± 0.19	98.66 ± 3.47	127	1.29 ± 0.12
central jet veto (20 GeV)	0.34 ± 0.01	0.06 ± 0.01	0.14 ± 0.03	0.05 ± 0.02	0.09 ± 0.06	61.20 ± 2.85	0.26 ± 0.09	−0.29 ± 0.19	63.98 ± 2.87	93	1.45 ± 0.16
Outside lepton veto	0.33 ± 0.01	0.05 ± 0.01	0.12 ± 0.03	0.04 ± 0.02	0.09 ± 0.06	43.48 ± 2.40	0.24 ± 0.09	−0.21 ± 0.16	46.13 ± 2.41	65	1.41 ± 0.19
ABCD Cuts	0.37 ± 0.01	0.09 ± 0.01	0.17 ± 0.04	0.06 ± 0.02	0.39 ± 0.12	116.35 ± 3.82	0.55 ± 0.25	−0.77 ± 0.21	119.66 ± 3.85	148	1.24 ± 0.11
Z control region (Z-peak)	0.21 ± 0.02	0.11 ± 0.01	30.18 ± 0.57	115.91 ± 1.35	1480.90 ± 7.86	112903.12 ± 142.89	14.91 ± 1.53	172.22 ± 10.28	115429.00 ± 143.52	119526	1.04 ± 0.00
b-jet veto	0.13 ± 0.01	0.09 ± 0.01	21.40 ± 0.47	74.67 ± 1.07	81.36 ± 1.79	81033.83 ± 120.71	10.53 ± 1.31	76.35 ± 8.34	81755.64 ± 121.04	80192	0.98 ± 0.00
$p_{T,tot} < 15$ GeV	0.09 ± 0.01	0.05 ± 0.01	16.06 ± 0.41	51.77 ± 0.91	43.27 ± 1.30	60545.82 ± 106.08	8.30 ± 1.19	21.80 ± 4.06	61047.61 ± 106.19	58830	0.96 ± 0.00
$m_{jj} > 500$ GeV	0.02 ± 0.00	0.00 ± 0.00	0.88 ± 0.08	2.01 ± 0.14	1.79 ± 0.27	1493.86 ± 14.60	0.22 ± 0.07	−0.34 ± 0.62	1545.83 ± 14.64	1989	1.29 ± 0.03
$\Delta Y_{jj} > 2.8$	0.02 ± 0.00	0.00 ± 0.00	0.75 ± 0.07	1.54 ± 0.12	1.60 ± 0.26	1156.65 ± 13.50	0.22 ± 0.07	−0.13 ± 0.55	1201.61 ± 13.53	1631	1.36 ± 0.04
central jet veto (20 GeV)	0.02 ± 0.00	0.00 ± 0.00	0.63 ± 0.07	1.16 ± 0.11	0.88 ± 0.19	754.28 ± 11.77	0.14 ± 0.05	−0.14 ± 0.44	794.68 ± 11.79	1123	1.41 ± 0.05
Outside lepton veto	0.02 ± 0.00	0.00 ± 0.00	0.46 ± 0.05	0.96 ± 0.10	0.67 ± 0.17	548.24 ± 10.70	0.11 ± 0.05	−0.49 ± 0.26	583.17 ± 10.72	794	1.36 ± 0.05
ABCD preselection	1.21 ± 0.02	0.28 ± 0.02	2.77 ± 0.13	1.85 ± 0.23	6.47 ± 0.51	666.20 ± 10.49	2.83 ± 0.59	−0.07 ± 0.60	696.17 ± 10.55	872	1.25 ± 0.05
A	0.63 ± 0.01	0.14 ± 0.01	0.47 ± 0.05	0.16 ± 0.08	1.15 ± 0.22	5.44 ± 0.74	0.71 ± 0.20	0.13 ± 0.17	8.28 ± 0.82	10	1.21 ± 0.40
B	0.00 ± 0.00	0.00 ± 0.00	0.36 ± 0.05	0.79 ± 0.08	0.68 ± 0.17	34.58 ± 2.59	0.02 ± 0.02	0.19 ± 0.15	37.17 ± 2.61	43	1.16 ± 0.19
C	0.37 ± 0.01	0.09 ± 0.01	0.17 ± 0.04	0.06 ± 0.02	0.39 ± 0.12	116.35 ± 3.82	0.55 ± 0.25	−0.77 ± 0.21	119.66 ± 3.85	148	1.24 ± 0.11
D	0.00 ± 0.00	0.00 ± 0.00	0.09 ± 0.02	0.37 ± 0.07	0.46 ± 0.14	454.14 ± 8.82	0.04 ± 0.03	0.43 ± 0.46	466.26 ± 8.84	604	1.30 ± 0.06

Table A.1: Cutflow for $ee/\mu\mu$

	VBF+VH [125 GeV]	ggF [125 GeV]	WW	other diboson	Top	$Z \to ee/\mu\mu$+jets	$Z \to \tau\tau$+jets	W+jets + QCD	Total Bkg.(+ggF)	Observed	Data/MC
Object selection	14.33 ± 0.14	82.31 ± 0.35	1883.46 ± 4.63	757.10 ± 7.13	8836.93 ± 19.02	340.21 ± 15.95	9403.66 ± 54.82	1582.88 ± 14.93	22891.74 ± 62.59	22852	1.00 ± 0.01
lepton p_{T}	14.15 ± 0.14	80.80 ± 0.35	1873.32 ± 4.61	714.22 ± 6.87	8805.61 ± 18.99	319.18 ± 15.61	8571.63 ± 52.59	1457.69 ± 14.85	21827.42 ± 60.49	22006	1.01 ± 0.01
OS leptons	13.10 ± 0.13	80.68 ± 0.35	1865.03 ± 4.60	356.27 ± 4.82	8752.22 ± 18.93	229.68 ± 13.13	8535.76 ± 52.49	959.00 ± 12.78	20783.56 ± 59.11	21143	1.02 ± 0.01
$m_{\ell\ell} > 12, 10$ GeV	13.05 ± 0.13	80.21 ± 0.35	1863.91 ± 4.60	341.53 ± 4.68	8748.47 ± 18.93	229.68 ± 13.13	8511.82 ± 52.45	952.24 ± 12.74	20732.77 ± 59.05	21109	1.02 ± 0.01
Z veto (for $ee, \mu\mu$)	13.05 ± 0.13	80.21 ± 0.35	1863.91 ± 4.60	341.53 ± 4.68	8748.47 ± 18.93	229.68 ± 13.13	8511.82 ± 52.45	952.24 ± 12.74	20732.77 ± 59.05	21109	1.02 ± 0.01
$\not{E}_T > 45$ GeV (SF)	13.05 ± 0.13	80.21 ± 0.35	1863.91 ± 4.60	341.53 ± 4.68	8748.47 ± 18.93	229.68 ± 13.13	8511.82 ± 52.45	952.24 ± 12.74	20732.77 ± 59.05	21109	1.02 ± 0.01
Scale factors					NF = 1.03						
at least two jets	6.65 ± 0.09	10.64 ± 0.13	143.23 ± 1.24	53.98 ± 1.79	7048.53 ± 17.48	18.87 ± 1.57	485.60 ± 8.78	98.04 ± 5.69	7861.82 ± 20.55	8042	1.02 ± 0.01
Scale factors					NF = 1.03		NF = 0.95				
b-jet veto	4.69 ± 0.07	7.57 ± 0.11	101.96 ± 1.04	39.07 ± 1.53	383.44 ± 3.96	13.52 ± 1.34	329.28 ± 7.05	48.99 ± 3.43	925.63 ± 9.08	949	1.03 ± 0.03
Scale factors					NF = 1.09		NF = 0.93				
$p_{\mathrm{T,tot}} < 15$ GeV	3.76 ± 0.06	4.83 ± 0.08	73.48 ± 0.88	26.65 ± 1.31	217.04 ± 3.06	7.68 ± 1.10	243.35 ± 6.20	9.32 ± 1.38	583.81 ± 7.30	619	1.06 ± 0.04
Scale factors					NF = 1.09		NF = 0.97				
$Z \to \tau\tau$ veto	3.18 ± 0.05	4.16 ± 0.08	43.35 ± 0.67	17.39 ± 1.07	141.38 ± 2.47	4.37 ± 0.88	88.65 ± 3.83	6.07 ± 1.06	305.68 ± 4.93	310	1.01 ± 0.06
Scale factors					NF = 1.18		NF = 1.40				
$m_{\mathrm{jj}} > 500$ GeV	1.14 ± 0.02	0.36 ± 0.02	2.90 ± 0.14	0.46 ± 0.16	7.18 ± 0.59	0.06 ± 0.06	2.32 ± 0.37	-0.01 ± 0.07	13.31 ± 0.73	13	0.98 ± 0.28
Scale factors					NF = 0.99		NF = 1.48				
$\Delta Y_{\mathrm{jj}} > 2.8$	1.12 ± 0.02	0.35 ± 0.02	2.57 ± 0.13	0.33 ± 0.13	5.37 ± 0.46	0.06 ± 0.06	1.31 ± 0.20	0.02 ± 0.07	10.05 ± 0.55	11	1.09 ± 0.34
Scale factors					NF = 1.21		NF = 1.55				
central jet veto (20 GeV)	1.04 ± 0.02	0.25 ± 0.02	2.23 ± 0.12	0.27 ± 0.12	3.47 ± 0.41	0	0.94 ± 0.18	0.04 ± 0.07	7.23 ± 0.49	8	1.11 ± 0.40
Scale factors					NF = 1.33		NF = 1.50				
Outside lepton veto	1.00 ± 0.02	0.23 ± 0.02	1.69 ± 0.10	0.18 ± 0.09	3.19 ± 0.41	0	0.56 ± 0.14	0.05 ± 0.07	5.93 ± 0.46	6	1.01 ± 0.42
Scale factors					NF = 1.33		NF = 1.50				
$\Delta\phi_{\ell\ell} < 1.8$	0.90 ± 0.02	0.20 ± 0.02	1.01 ± 0.08	0.15 ± 0.09	1.85 ± 0.31	0	0.29 ± 0.11	0.07 ± 0.05	3.60 ± 0.36	4	1.11 ± 0.57
Scale factors					NF = 1.33		NF = 1.50				
$m_{\ell\ell} < 50$ GeV	0.77 ± 0.02	0.18 ± 0.02	0.41 ± 0.05	0.04 ± 0.03	0.73 ± 0.20	0	0.21 ± 0.10	0.04 ± 0.04	1.62 ± 0.24	2	1.23 ± 0.89
Scale factors					NF = 1.33		NF = 1.50				
$m_{\mathrm{T}} < 130$ GeV	0.71 ± 0.01	0.16 ± 0.02	0.19 ± 0.04	0.01 ± 0.01	0.35 ± 0.14	0	0.07 ± 0.05	0.01 ± 0.01	0.80 ± 0.15	0	0
Top control region ($n_{bjets} = 1$)	1.65 ± 0.05	2.59 ± 0.06	35.35 ± 0.64	13.10 ± 0.88	2351.21 ± 9.80	4.66 ± 0.74	119.91 ± 4.34	32.91 ± 3.57	2560.64 ± 11.37	2619	1.02 ± 0.02
$p_{\mathrm{T,tot}} < 15$ GeV	1.22 ± 0.04	1.46 ± 0.05	22.63 ± 0.51	7.78 ± 0.67	1328.79 ± 7.35	2.54 ± 0.57	79.20 ± 3.71	1.68 ± 1.13	1444.78 ± 8.37	1569	1.09 ± 0.03
$Z \to \tau\tau$ veto	1.01 ± 0.04	1.26 ± 0.05	12.72 ± 0.38	4.98 ± 0.57	863.00 ± 5.93	1.29 ± 0.42	29.04 ± 2.28	0.92 ± 0.76	913.42 ± 6.44	992	1.09 ± 0.04
$m_{\mathrm{jj}} > 500$ GeV	0.20 ± 0.01	0.05 ± 0.01	0.80 ± 0.07	0.34 ± 0.14	29.43 ± 1.10	0	0.90 ± 0.18	-0.04 ± 0.07	31.48 ± 1.13	37	1.18 ± 0.20
$\Delta Y_{\mathrm{jj}} > 2.8$	0.20 ± 0.01	0.04 ± 0.01	0.59 ± 0.06	0.15 ± 0.05	21.69 ± 0.94	0	0.54 ± 0.12	-0.08 ± 0.05	22.93 ± 0.96	25	1.09 ± 0.22
central jet veto (20 GeV)	0.17 ± 0.01	0.02 ± 0.01	0.42 ± 0.05	0.08 ± 0.04	8.39 ± 0.59	0	0.22 ± 0.08	-0.02 ± 0.04	9.11 ± 0.60	12	1.32 ± 0.39
Outside lepton veto	0.16 ± 0.01	0.02 ± 0.01	0.32 ± 0.04	0.08 ± 0.04	5.22 ± 0.46	0	0.14 ± 0.06	0.00 ± 0.04	5.77 ± 0.47	7	1.21 ± 0.47
$Z \to \tau\tau$ control region	0.28 ± 0.02	0.31 ± 0.02	2.26 ± 0.16	1.18 ± 0.29	5.72 ± 0.47	0.70 ± 0.27	100.68 ± 4.05	0.35 ± 0.48	111.90 ± 4.13	116	1.04 ± 0.10
Z control region (lowMET, lowMll)	1.95 ± 0.05	3.49 ± 0.07	5.59 ± 0.25	9.49 ± 0.87	304.05 ± 3.57	2.58 ± 0.65	126.69 ± 4.57	30.25 ± 2.54	482.69 ± 6.42	527	1.09 ± 0.05
b-jet veto	1.40 ± 0.04	2.47 ± 0.06	4.08 ± 0.21	6.80 ± 0.72	14.96 ± 0.76	1.69 ± 0.54	89.43 ± 3.81	19.43 ± 1.95	139.18 ± 4.44	148	1.06 ± 0.09
$p_{\mathrm{T,tot}} < 15$ GeV	1.12 ± 0.03	1.59 ± 0.05	3.07 ± 0.18	4.81 ± 0.62	8.17 ± 0.56	1.07 ± 0.48	70.21 ± 3.47	2.79 ± 0.74	91.97 ± 3.69	104	1.13 ± 0.12
$m_{\mathrm{jj}} > 500$ GeV	0.34 ± 0.01	0.12 ± 0.01	0.14 ± 0.04	0.02 ± 0.01	0.30 ± 0.11	0	0.23 ± 0.07	-0.02 ± 0.04	0.78 ± 0.14	8	10.20 ± 4.05
$\Delta Y_{\mathrm{jj}} > 2.8$	0.34 ± 0.01	0.12 ± 0.01	0.13 ± 0.03	0.02 ± 0.01	0.30 ± 0.11	0	0.19 ± 0.06	-0.02 ± 0.04	0.73 ± 0.14	8	10.92 ± 4.37
central jet veto (20 GeV)	0.32 ± 0.01	0.08 ± 0.01	0.12 ± 0.03	0.00 ± 0.00	0.21 ± 0.09	0	0.09 ± 0.05	-0.01 ± 0.02	0.50 ± 0.11	5	10.09 ± 5.07
Outside lepton veto	0.31 ± 0.01	0.08 ± 0.01	0.10 ± 0.03	0.00 ± 0.00	0.17 ± 0.09	0	0.06 ± 0.04	-0.01 ± 0.02	0.39 ± 0.10	4	10.17 ± 5.73
ABCD Cuts	0.34 ± 0.01	0.12 ± 0.01	0.14 ± 0.04	0.02 ± 0.01	0.30 ± 0.11	0	0.23 ± 0.07	-0.02 ± 0.04	0.78 ± 0.14	8	10.20 ± 4.05
Z control region (Z-peak)	6.65 ± 0.09	10.64 ± 0.13	143.23 ± 1.24	53.98 ± 1.79	6831.12 ± 16.94	18.87 ± 1.57	485.60 ± 8.78	98.04 ± 5.69	7644.41 ± 20.09	8042	1.05 ± 0.01
b-jet veto	4.69 ± 0.07	7.57 ± 0.11	101.96 ± 1.04	39.07 ± 1.53	371.61 ± 3.84	13.52 ± 1.34	347.94 ± 7.45	48.99 ± 3.43	932.46 ± 9.34	949	1.02 ± 0.03
$p_{\mathrm{T,tot}} < 15$ GeV	3.76 ± 0.06	4.83 ± 0.08	73.48 ± 0.88	26.65 ± 1.31	198.84 ± 2.80	7.68 ± 1.10	261.77 ± 6.66	9.32 ± 1.38	584.03 ± 7.61	619	1.06 ± 0.04
$m_{\mathrm{jj}} > 500$ GeV	1.36 ± 0.02	0.41 ± 0.02	5.31 ± 0.19	0.96 ± 0.24	9.71 ± 0.62	0.15 ± 0.11	6.76 ± 0.62	-0.02 ± 0.16	23.55 ± 0.95	35	1.49 ± 0.26
$\Delta Y_{\mathrm{jj}} > 2.8$	1.34 ± 0.02	0.39 ± 0.02	4.56 ± 0.18	0.72 ± 0.19	8.41 ± 0.58	0.15 ± 0.11	5.06 ± 0.52	0.03 ± 0.16	19.55 ± 0.85	23	1.18 ± 0.25
central jet veto (20 GeV)	1.23 ± 0.02	0.28 ± 0.02	3.88 ± 0.16	0.48 ± 0.15	4.32 ± 0.41	0.09 ± 0.09	3.41 ± 0.48	-0.05 ± 0.09	12.62 ± 0.69	18	1.43 ± 0.35
Outside lepton veto	1.19 ± 0.02	0.26 ± 0.02	2.87 ± 0.13	0.36 ± 0.13	3.37 ± 0.37	0.09 ± 0.09	2.57 ± 0.46	-0.01 ± 0.09	9.71 ± 0.63	13	1.34 ± 0.38
ABCD preselection	1.14 ± 0.02	0.36 ± 0.02	2.90 ± 0.14	0.46 ± 0.16	6.07 ± 0.50	0.06 ± 0.06	1.65 ± 0.27	-0.01 ± 0.07	11.53 ± 0.61	13	1.13 ± 0.32
A	0.57 ± 0.01	0.17 ± 0.02	0.51 ± 0.06	0.06 ± 0.03	1.33 ± 0.23	0.06 ± 0.06	0.80 ± 0.23	0.01 ± 0.04	2.97 ± 0.34	2	0.67 ± 0.48
B	0.00 ± 0.00	0	0.56 ± 0.07	0.00 ± 0.00	0.87 ± 0.18	0	0	-0.00 ± 0.00	1.43 ± 0.19	0	0
C	0.34 ± 0.01	0.12 ± 0.01	0.14 ± 0.04	0.02 ± 0.01	0.30 ± 0.11	0	0.23 ± 0.07	-0.02 ± 0.04	0.78 ± 0.14	8	10.20 ± 4.05
D	0.00 ± 0.00	0.00 ± 0.00	0.12 ± 0.03	0.12 ± 0.09	0.11 ± 0.07	0	0.04 ± 0.03	0.02 ± 0.03	0.42 ± 0.13	0	0

Table A.2: Cutflow for $e\mu/\mu e$

Bibliography

[1] Ch. Kraus, B. Bornschein, L. Bornschein, J. Bonn, B. Flatt, et al. Final results from phase II of the Mainz neutrino mass search in tritium beta decay. *Eur.Phys.J.*, C40:447–468, 2005.

[2] P.A.R. Ade et al. Planck 2013 results. XVI. Cosmological parameters. *Astron.Astrophys.*, 2014.

[3] J. Beringer et al. Review of particle physics. *Phys. Rev. D*, 86:010001, 2012.

[4] David Griffiths. *Introduction to Elementary Particles*. Wiley, 1987.

[5] A. Zee. *Quantum Field Theory in a Nutshell*. Princeton University Press, 2003.

[6] Michael Edward Peskin and Daniel V. Schroeder. *An Introduction To Quantum Field Theory*. Westview Press, 1995.

[7] F. Englert and R. Brout. Broken Symmetry and the Mass of Gauge Vector Mesons. *Physical Review Letters*, 13:321–323, August 1964.

[8] P. W. Higgs. Broken Symmetries and the Masses of Gauge Bosons. *Physical Review Letters*, 13:508–509, October 1964.

[9] G. S. Guralnik, C. R. Hagen, and T. W. Kibble. Global Conservation Laws and Massless Particles. *Physical Review Letters*, 13:585–587, November 1964.

[10] Sheldon L. Glashow. Partial-symmetries of weak interactions. *Nuclear Physics*, 22(4):579 – 588, 1961.

[11] Steven Weinberg. A model of leptons. *Phys. Rev. Lett.*, 19:1264–1266, Nov 1967.

[12] Abdus Salam. Weak and Electromagnetic Interactions. *Conf.Proc.*, C680519:367–377, 1968.

[13] Yuri L. Dokshitzer, Valery A. Khoze, and T. Sjostrand. Rapidity gaps in Higgs production. *Phys.Lett.*, B274:116–121, 1992.

[14] LHC Higgs Cross Section Working Group Figures. https://twiki.cern.ch/twiki/bin/view/LHCPhysics/CrossSectionsFigures. Accessed: 2014-09-11.

[15] LHC Higgs Cross Section Working Group, S. Heinemeyer, C. Mariotti, G. Passarino, and R. Tanaka (Eds.). Handbook of LHC Higgs Cross Sections: 3. Higgs Properties. *CERN-2013-004*, CERN, Geneva, 2013.

[16] ATLAS Collaboration. Observation of a new particle in the search for the Standard Model Higgs boson with the ATLAS detector at the LHC. *Physics Letters B*, 716(1):1 – 29, 2012.

[17] CMS Collaboration. Observation of a new boson at a mass of 125 GeV with the CMS experiment at the LHC. *Physics Letters B*, 716(1):30 – 61, 2012.

[18] The ATLAS Collaboration. Measurements of the properties of the Higgs-like boson in the $WW^{(*)} \to \ell\nu\ell\nu$ decay channel with the ATLAS detector using 25 fb^{-1} of proton-proton collision data. Technical Report ATLAS-CONF-2013-030, CERN, Geneva, Mar 2013. Available as: https://cds.cern.ch/record/1527126.

[19] Evidence for a particle decaying to W+W- in the fully leptonic final state in a standard model Higgs boson search in pp collisions at the LHC. Technical Report CMS-PAS-HIG-13-003, CERN, Geneva, 2013. Available as: https://cds.cern.ch/record/1523673.

[20] Evidence for Higgs Boson Decays to the $\tau^+\tau^-$ Final State with the ATLAS Detector. Technical Report ATLAS-CONF-2013-108, CERN, Geneva, Nov 2013. Available as: https://cds.cern.ch/record/1632191.

[21] The CMS Collaboration. Evidence for the 125 GeV Higgs boson decaying to a pair of τ leptons. *Journal of High Energy Physics*, 2014(5), 2014.

[22] Lyndon Evans and Philip Bryant. LHC Machine. *Journal of Instrumentation*, 3(08):S08001, 2008.

[23] The ATLAS Collaboration et al. The ATLAS Experiment at the CERN Large Hadron Collider. *Journal of Instrumentation*, 3(08):S08003, 2008.

[24] The LHC's first long run. http://cerncourier.com/cws/article/cern/54381. Accessed: 2014-09-02.

[25] ATLAS Luminosity Public Results. https://twiki.cern.ch/twiki/bin/view/AtlasPublic/LuminosityPublicResults. Accessed: 2014-09-02.

[26] The HSG3 Working Group. Analysis of $H \to WW \to \ell\nu\ell\nu$ ggF and VBF production modes with 20 fb^{-1} and 5 fb^{-1} of data collected with the ATLAS detector at $\sqrt{s} = 8$ and 7 TeV. Technical Report ATL-COM-PHYS-2014-466, CERN, Geneva, May 2014. Internal supporting note.

[27] Performance of the ATLAS Electron and Photon Trigger in p-p Collisions at $\sqrt{s} =$ 7 TeV in 2011. Technical Report ATLAS-CONF-2012-048, CERN, Geneva, May 2012. Available as: `http://cds.cern.ch/record/1450089`.

[28] Performance of the ATLAS muon trigger in 2011. Technical Report ATLAS-CONF-2012-099, CERN, Geneva, Jul 2012. Available as: `http://cds.cern.ch/record/1462601`.

[29] V.N. Ivanchenko. Geant4 toolkit for simulation of HEP experiments. *Nucl.Instrum.Meth.*, A502:666–668, 2003.

[30] W Lukas. Fast Simulation for ATLAS: Atlfast-II and ISF. Technical Report ATL-SOFT-PROC-2012-065, CERN, Geneva, Jun 2012. Available as: `http://cds.cern.ch/record/1458503`.

[31] Simone Alioli, Paolo Nason, Carlo Oleari, and Emanuele Re. A general framework for implementing NLO calculations in shower Monte Carlo programs: the POWHEG BOX. *JHEP*, 1006:043, 2010.

[32] Torbjorn Sjostrand, Stephen Mrenna, and Peter Z. Skands. PYTHIA 6.4 Physics and Manual. *JHEP*, 0605:026, 2006.

[33] Torbjörn Sjöstrand, Stephen Mrenna, and Peter Skands. A brief introduction to PYTHIA 8.1. *Computer Physics Communications*, 178(11):852 – 867, 2008.

[34] Gennaro Corcella, Ian G. Knowles, Giuseppe Marchesini, Stefano Moretti, Kosuke Odagiri, Peter Richardson, Michael H. Seymour, and Bryan R. Webber. HERWIG 6: an event generator for hadron emission reactions with interfering gluons (including supersymmetric processes). *Journal of High Energy Physics*, 2001(01):010, 2001.

[35] T. Binoth, M. Ciccolini, N. Kauer, and M. Kramer. Gluon-induced W-boson pair production at the LHC. *JHEP*, 0612:046, 2006.

[36] Michelangelo L. Mangano, Mauro Moretti, Fulvio Piccinini, Roberto Pittau, and Antonio D. Polosa. ALPGEN, a generator for hard multiparton processes in hadronic collisions. *JHEP*, 0307:001, 2003.

[37] T. Gleisberg, Stefan. Hoeche, F. Krauss, M. Schonherr, S. Schumann, et al. Event generation with SHERPA 1.1. *JHEP*, 0902:007, 2009.

[38] Borut Paul Kersevan and Elzbieta Richter-Was. The Monte Carlo event generator AcerMC versions 2.0 to 3.8 with interfaces to PYTHIA 6.4, HERWIG 6.5 and ARIADNE 4.1. *Comput.Phys.Commun.*, 184:919–985, 2013.

[39] Matteo Cacciari, Gavin P. Salam, and Gregory Soyez. The anti-k_t jet clustering algorithm. *Journal of High Energy Physics*, 2008(04):063, 2008.

[40] Calibration of the performance of *b*-tagging for *c* and light-flavour jets in the 2012 ATLAS data. Technical Report ATLAS-CONF-2014-046, CERN, Geneva, Jul 2014. Available as: `https://cds.cern.ch/record/1741020`.

[41] Aaron Roodman. Blind analysis in particle physics. *eConf*, C030908:TUIT001, 2003.

[42] Procedure for the LHC Higgs boson search combination in Summer 2011. Technical Report CMS-NOTE-2011-005. ATL-PHYS-PUB-2011-11, CERN, Geneva, Aug 2011. Available as: `https://cds.cern.ch/record/1375842`.

[43] Glen Cowan, Kyle Cranmer, Eilam Gross, and Ofer Vitells. Asymptotic formulae for likelihood-based tests of new physics. *Eur.Phys.J.*, C71:1554, 2011.

Acknowledgements

Ich möchte mich bei folgenden Personen bedanken, die mich bei dieser Arbeit unterstützt haben:

- Prof. Dorothee Schaile für die Möglichkeit an ihrem Lehrstuhl zu arbeiten.
- Dr. Johannes Elmsheuser für hilfreiches Feedback während allen Phasen der Arbeit und für die ausgezeichnete Betreuung.
- Frau Grimm-Zeidler für die Hilfe bei allen Formalitäten und organisatorischen Fragen.
- Bonnie Chow für die großartige Zusammenarbeit, die Hilfe bei allen Fragen und die wunderbaren Diskussionen über die exakten Details der technischen Implementierung der Analyse.
- Allen Mitgliedern der Higgs Gruppe des Lehrstuhls, insbesondere Christian Meineck, Friedrich Hönig und meinem Bürokollegen Thomas Maier für die angenehme Atmosphäre und die Hilfe bei technischen Problemen.
- Allen Mitgliedern des Lehrstuhls für das gute Arbeitsklima, die Diskussionen beim Mittagessen und Kaffee und das Tischtennisspiel in den Zeiten bevor die Baumaßnahmen begannen
- I would like to thank the conveners and members of the ATLAS HSG3 group and the VBF subgroup for giving me the opportunity to contribute to an exciting analysis.
- Besonderer Dank geht an meine Eltern, die mich während meines gesamten Studiums emotional und finanziell unterstützt haben.
- Zuletzt möchte ich meiner Freundin Lydia Krug danken, die immer für mich da ist und mich auch in verwirrten Geisteszuständen kurz vor Deadlines ausgehalten hat

"In the meantime ... Thanks, ants - Thants"

Look around You, Episode 3
Robert Popper, Peter Serafinowicz

Erklärung

Hiermit erkläre ich, die vorliegende Arbeit selbständig verfasst zu haben und keine anderen als die in der Arbeit angegebenen Quellen und Hilfsmittel benutzt zu haben.

München, den 6.10.2014

_____

(Nikolai Hartmann)